

A Coupled Ground Heat Flux-Surface Energy Balance Model of Evaporation Using Thermal Remote Sensing Observations

Devansh Desai^{1,11*}, Kaniska Mallick^{2,10*}, Bimal K. Bhattacharya³, Ganapati S. Bhat⁴, Ross Morrison⁵, Jamie Clevery⁶, Will Woodgate⁷, Jason Beringer⁸, Kerry Cawse-Nicholson⁹, Siyan Ma¹⁰, Joseph Verfaillie¹⁰, Dennis Baldocchi¹⁰

¹Department of Physics, Electronics & Space Sciences, Gujarat University, Ahmedabad, India

²Remote Sensing and Natural Resources Modeling, Department ERIN, Luxembourg Institute of Science and Technology, Belvaux, L4422, Luxembourg

³Agriculture & land Ecosystem Division, Space Applications Center, ISRO, Ahmedabad, India

⁴Centre for Atmosphere and Oceanic Studies, Indian Institute of Sciences, Bengaluru, India

⁵Centre for Ecology and Hydrology, Lancaster, UK

⁶Terrestrial Ecosystem Research Network, College of Science and Engineering, James Cook University, Cairns, Queensland

⁷CSIRO Land and Water, Private Bag 5, Floreat 6913, Western Australia.

⁸School of Earth and Environment (SEE), The University of Western Australia, WA, 6009, Australia

⁹Carbon Cycles and Ecosystems, Jet Propulsion Laboratory, California Institute of Technology, United States

¹⁰Environmental Science Policy and Management, University of California, Berkeley, United States

¹¹Department of Physics, Institute of Science, Silver Oak University, Ahmedabad, Gujarat, India

Corresponding authors: Kaniska Mallick (kaniska.mallick@gmail.com) and Devansh Desai (ddesai10793@gmail.com)

31 **Abstract**

32 ~~One of the major~~The major undetermined problems in evaporation (ET) retrieval using thermal
33 infrared (TIR) remote sensing is the lack of a physically based ground heat flux (G) model and its
34 ~~amalgamation-integration~~ with the surface energy balance (SEB) model. Here, we present a novel
35 approach based on coupling a thermal inertia (TI)-based mechanistic G model with an analytical
36 ~~surface energy balance model, Surface Temperature Initiated Closure (STIC, version STIC1.2).~~
37 ~~SEB model (Surface Temperature Initiated Closure) (STIC, version STIC1.2).~~ The coupled model
38 is named ~~as~~STIC-TI and it uses noon-night (1:30 pm and am) land surface temperature (T_s),
39 surface albedo, and vegetation index from MODIS Aqua in conjunction with a clear-sky net
40 radiation model and ancillary meteorological information. ~~The~~SEB flux estimates from STIC-TI
41 were evaluated with respect to the *in-situ* fluxes from Eddy Covariance (EC) measurements in
42 diverse agriculture and natural ecosystems of contrasting aridity in ~~the-both~~ northern and southern
43 hemispheres. ~~(e.g., India, United States of America) and southern hemisphere (e.g., Australia).~~
44 Sensitivity analysis revealed substantial sensitivity of the STIC-TI-derived fluxes due to T_s
45 uncertainty, ~~and partial compensation of sensitivity of G to T_s due to the nature of the equations~~
46 ~~used in the TI-based G model. An evaluation of noontime G (G_i) estimates showed 12-21% error~~
47 ~~across six flux tower sites in both the hemispheres and a comparison between STIC-TI versus other~~
48 ~~G models also revealed the substantially better performance of the former. An evaluation of STIC-~~
49 ~~TI G estimates with respect to in-situ measurements showed an error range of 12-21% across six~~
50 ~~flux tower sites in both the hemispheres. A comparison of STIC-TI G estimates with other G~~
51 ~~models revealed substantially better performance of the former.~~ While the instantaneous noontime
52 net radiation (R_{Ni}) and latent heat flux (LE_i) was overestimated (15% and 25%), sensible heat flux
53 (H_i) was underestimated (22%). ~~with error of 22%.~~The errors in G_i were associated with the errors
54 in daytime T_s and mismatch of footprint between the model estimates and measurements.
55 Overestimation (underestimation) of LE_i (H_i) was associated with the overestimation of net
56 available energy (R_{Ni} - G_i) and use of unclosed surface energy balance~~SEB~~ measurements. The
57 deviations of STIC-TI heat flux estimates from measurements were found to be restricted within -
58 40° to 30° day view angle, while no impact of night view angle was evident. Being independent
59 of any leaf-scale conductance parameterization and having a coupled sub-model of G, STIC-TI
60 can make a valuable contribution to mapping and monitoring ecosystem water stress and

61 evaporation in the terrestrial ecosystems using noon-night thermal infrared observations from
62 existing and future EO missions such as INSAT 4th generation and TRISHNA.

63 **Keywords:** Thermal remote sensing, water stress, evaporation, ground heat flux, thermal inertia,
64 surface energy balance, STIC, terrestrial ecosystem

65 **1 Introduction**

66 One of the outstanding challenges in evaporation (ET) estimation through surface energy balance
67 (SEB) model concerns an accurate characterization of ground heat flux in the open canopy system
68 with mixed vegetation such as savanna or in ecosystems with low mean fractional vegetation
69 cover, prevailing water stress, and strong seasonality in soil moisture. Ground heat flux (G) is an
70 intrinsic component of the surface energy balance (Sauer and Horton, 2005), affecting the net
71 available energy for evaporation (ET) (the equivalent water depth of latent heat flux, LE) and
72 sensible heat flux. It represents an energy flow path that couples surface with atmosphere and has
73 important implications for the underlying thermal regime (Sauer and Horton, 2005). Depending
74 on the vegetation fraction and water stress, the magnitude of instantaneous G varies greatly across
75 different ecosystems. In the humid ecosystems with predominantly dense canopies and high mean
76 fractional vegetation cover, G contributes to a small proportion in the surface energy balance.
77 Dense canopy cover leads to less transmission of radiative fluxes through multiple layers of
78 canopies, which results in low warming of the soil floor. Due to persistently high soil water
79 content, humid ecosystems generally show low diurnal and seasonal variability in G. By contrast,
80 the magnitude of G is substantially large in arid and semi-arid ecosystems with sparse and open
81 canopy and soil moisture deficits. Evaporation is also an integral component of the surface energy
82 balance where water is lost from and within the soil-vegetation-substrate complex through the
83 ‘physics of evaporation and ‘ecophysiology’ of transpiration while regulating the temperature and
84 growth of vegetation (Martel et al., 2018). Due to complex feedback between the physics of ground
85 heat flux, land-atmosphere interactions and vegetation ecophysiology, evaporation modelling ~~at~~
86 different space-time scales in the complex ecosystems remained a challenging task (Wang et al.,
87 2013; Kiptala et al., 2013). This paper addresses the challenge of simultaneous estimation of G
88 and ET by combining thermal remote sensing observations with a mechanistic G model and
89 analytical surface energy balance (SEB) model.

90 SEB models mainly emphasize on estimating sensible heat flux (H) by resolving the aerodynamic
91 conductance (g_A) and computes LE as a residual SEB component as follows:

$$LE = R_N - G - H \quad (1)$$

92 R_N is the net radiation. The proportion of R_N that is partitioned into G depends upon soil properties
93 like its albedo, soil moisture, soil thermal properties such as thermal conductivity and heat
94 capacity, which vary with mineral, organic and soil water fractions. SEB models use land surface
95 temperature (LST or T_s) as an important lower boundary condition for estimating H and LE. Due
96 to the extraordinarily high sensitivity of T_s to evaporative cooling and soil water content variations,
97 thermal infrared (TIR) remote sensing is extensively used in large scale evaporation diagnostics
98 (Kustas and Anderson, 2009; Mallick et al., 2014, 2015a, 2018a; Cammalleri and Vogt, 2015;
99 Anderson et al., 2012). Evaporation estimation through SEB models commonly employ empirical
100 sub-models of G in a stand-alone mode. Despite the utility of mechanistic G models is
101 demonstrated in different studies (Verhoef, 2004; Murray and Verhoef, 2007; Verhoef et al.,
102 2012), no TIR-based evaporation study attempted to couple a mechanistic G model with a SEB
103 model. Land surface temperature (LST or T_s) retrieved through thermal infrared (TIR) remote
104 sensing carries imprints of soil water content and is extraordinarily sensitive to evaporative
105 cooling, which makes it a crucial variable for estimating sensible heat flux (H) ET through the
106 SEB models (Kustas and Anderson, 2009; Mallick et al., 2014, 2015a, 2018a; Cammalleri and
107 Vogt, 2015; Anderson et al., 2012). However, it is the aerodynamic temperature (T_0) that is
108 responsible for the sensible heat transfer and the inequality of T_s versus T_0 introduces additional
109 uncertainty in ET retrieval through the SEB models. The differences between T_s and T_0 is
110 accommodated either by using two source approximation of SEB (Anderson et al., 2012) or
111 through an empirical extra resistance in the single source SEB models (Su, 2002). In the SEB
112 method, T_s represents the lower boundary condition to estimate both sensible (H) and latent heat
113 fluxes (LE) (Anderson et al., 2012; Mallick et al., 2014, 2015a, 2018a). SEB models mainly
114 emphasize on estimating H by resolving the aerodynamic conductance (g_A) and resolves LE as a
115 residual SEB component as follows:

$$LE = R_N - G - H \quad (1)$$

116 R_N is the net radiation. The proportion of R_N that is partitioned into conductive heat flux (G)
117 depends upon soil properties like its albedo, soil moisture, soil thermal properties such as heat
118 conductance and capacity, which vary with mineral, organic and water fractions. The magnitude
119 of G varies greatly across different ecosystems from as low as $< 20 \text{ W m}^{-2}$ under dense forest to as
120 high as 100 W m^{-2} over dry soils in arid and semi-arid landscapes or the rows between crops. In
121 the humid ecosystems with predominantly dense canopies and high mean fractional vegetation
122 cover, G contributes to a small proportion in eq. (1). Dense canopy cover leads to less transmission
123 of downwelling shortwave radiation flux through multiple layers of canopies, which results in low
124 warming of the soil floor. Due to persistently high soil water content, humid ecosystems generally
125 show low diurnal and seasonal variability in G . By contrast, the magnitude of G is substantially
126 large in the arid and semi-arid ecosystems with sparse and open canopy and high water stress. One
127 of the outstanding challenges in SEB modeling concerns an accurate estimation of G in the open
128 canopy system such as savanna with mixed vegetation or in ecosystems with low mean fractional
129 vegetation cover, predominant water stress, and strong seasonality in soil moisture.

130 While the utility of a surface heat capacity and thermal inertia (TI) based mechanistic G model
131 was demonstrated by Murray and Verhoef (2007), Verhoef et al. (2012), and Mallick et al. (2015b);
132 the potential of an analytical SEB model (Mallick et al., 2014, 2015, 2016, 2018a,b) for mapping
133 ET in a variety of ecological transects was also demonstrated by Bhattarai et al. (2018, 2019).
134 Recognizing the significant conclusions of Verhoef et al. (2012), Mallick et al. (2014; 2015a,b;
135 2016; 2018a,b) and Bhattarai et al. (2018, 2019), there is a need to overcome the challenges of
136 accurate G estimation and to complement the overarching gaps in SEB modeling in the sparsely
137 vegetated open canopy systems. Present study coupled the TI-based G model of Murray and
138 Verhoef (2007), after required modification, with the current version of an analytical ET model,
139 the Surface Temperature Initiated Closure (STIC, version 1.2; Mallick et al., 2014, 2015a, 2016,
140 2018a,b) and evaluated this new coupled G -SEB model in different ecosystems of contrasting
141 aridity.

142 The SEB models for ET estimation driven by remote sensing observations Remote sensing based
143 ET models generally use linear and non-linear relationships for estimating G and such methods
144 generally employ R_N , T_s , albedo (α_R), and NDVI (e.g., Bastiaanssen et al., 1998; Friedl, 2002;
145 Santanello and Friedl, 2003). While the inclusion of T_s and albedo serves as a proxy for soil

146 moisture and surface characteristics effects in G, inclusion of NDVI provides a scaling of G - R_N
147 ratio for different fractional vegetation cover. Unfortunately, all the approaches are empirical and
148 do not include any information of ~~deep~~ soil temperature or daily temperature amplitude. ~~as lower~~
149 ~~boundary conditions~~. These empirical model functions also lack the universal consensus. Setting
150 G as a fraction of R_N does not solve the energy balance equation and disregards the role of thermal
151 inertia of the land surface (Mallick et al., 2015b). This could introduce substantial uncertainty in
152 LE estimation because G effectively couples the surface energy balance with energy transfer
153 processes in the soil thermal regime. It provides physical feedback to LE through the effects of
154 soil moisture, temperature, and conductivity (thermal and hydraulic) (Sauer and Horton, 2005).
155 Such feedbacks are most critical in the arid and semi-arid ecosystems where LE is significantly
156 constrained by the soil moisture dry-down. The limits imposed on LE by the water stress
157 consequently result in greater partitioning of the net available energy (i.e., $R_N - G$) into H and G
158 (Castelli et al., 1999).

159 When LE is reduced due to soil moisture dry-down, both G and T_s tend to show rapid intra-
160 seasonal rise. ~~When LE is reduced due to soil moisture dry-down and water stress, both G and T_s~~
161 ~~tend to show rapid rise.~~ Therefore, the surface energy balance equation could be linked with
162 mechanistic G model, T_s harmonics (Verhoef, 2004), and soil moisture availability. Realizing the
163 importance of direct estimates of G in LE and invigorated by the advent of TIR remote sensing,
164 Verhoef et al., (2012) demonstrated the potential of a TI-based mechanistic model (Murray and
165 Verhoef, 2007) (MV2007 hereafter) for spatio-temporal G estimates in the semi-arid ecosystems
166 of Africa. Some studies also emphasized the importance of using noontime and nighttime T_{sday} -
167 night T_s and R_N for estimating G (Mallick et al., 2015b; Bennet et al., 2008; Tsuang, 2005). The
168 method of MV2007 has so far been tested in a stand-alone mode, and no remote sensing method
169 has so far been~~is so far~~ attempted to combine such a mechanistic G model (e.g., MV2007-TI
170 model) with a SEB model for coupled energy-water flux estimation and validation.

171 By integrating T_s into a combined structure of the Penman-Monteith (PM) and Shuttleworth-
172 Wallace (SW) model, an analytical SEB modeling was proposed by Mallick et al., (2014, 2015a,
173 2016). The model, Surface Temperature Initiated Closure (STIC), is based on finding analytical
174 solution for aerodynamic and canopy-surface conductance (g_A and g_S) where the expressions of
175 the conductances were constrained with an aggregated water stress factor. Through physically

176 linking water stress (T_s derived) with g_A and g_s , STIC established a direct feedback between T_s ,
177 H and LE, and simultaneously overcame the need of empirical parameterization for estimating the
178 conductances (Mallick et al., 2016, 2018a). Different versions of STIC have been extensively
179 validated in different ecological transects (Tropical rainforest to woody savanna) and aridity
180 gradients (humid to arid) (Trebs et al., 2021; Bai et al., 2021; Mallick et al., 2015a; 2016; 2018a,
181 b; Bhattarai et al., 2018, 2019). Based on the conclusions of Verhoef et al. (2012), Mallick et al.
182 (2014; 2015a,b; 2016; 2018a,b, 2022), Bhattarai et al. (2018, 2019), and Bai et al. (2021), there is
183 a need to address some of the challenges in SEB modeling, which are, (i) accurate estimation of G
184 and ET in sparse vegetation, (ii) testing the utility of coupling a TI-based G model with an
185 analytical SEB model for accurately estimating G and ET, and (iii) detailed evaluation of a coupled
186 G-SEB model at the ecosystem scale. Realizing the significance of mechanistic G model
187 (MV2007), the advantage of the analytical STIC model, and to mitigate some of the overarching
188 gaps in SEB modeling in sparsely vegetated open canopy systems, this study presents the first-
189 ever coupled implementation of MV2007 G with the most recent version of STIC (STIC1.2).
190 ~~Realizing the significance of mechanistic G model (MV2007) and the advantage of analytical~~
191 ~~solution for different turbulent heat fluxes and conductances from the STIC model, this paper~~
192 ~~presents the first ever coupled implementation of MV2007 G with the most recent version of STIC~~
193 ~~(STIC1.2).~~ We name this new coupled model as STIC-TI and it requires daynoon-night T_s and
194 associated remotely sensed land surface variables as inputs. We performed subsequent evaluation
195 of STIC-TI in nine terrestrial ecosystems in arid, semi-arid and sub-humid climate in India, the
196 United States of America (USA) (representing northern hemisphere) and Australia (representing
197 southern hemisphere) at the eddy covariance flux tower sites. The current study addresses the
198 following research questions and objectives:

- 199 (i) What is the performance of STIC-TI G estimates when compared with conventionally used
200 empirical G models~~ontemporary empirical models~~ in ecosystems having low mean fractional
201 vegetation cover (f_c) (≤ 0.5) and having larger soil exposure to radiation for example in
202 Savanna?
- 203 (ii) How do the estimates from STIC-TI LE and H fluxes compare with LE and H observations in
204 diverse terrestrial ecosystems that represent a varied range of f_c (0.25 – 0.5) covering cropland,
205 savanna, mulga vegetation (woodlands and open-forests dominated by the mulga tree [Acacia

206 aneura) spread across arid, semi-arid, sub-humid, humid climates over a vast range of rainfall
207 (250 to 1730 mm), temperature (-4 to 46°C) and soil regimes?

208 (iii) What is the seasonal variability of G and evaporative fraction from STIC-TI model in a wide
209 range of ecosystems having contrasting aridity and vegetation cover?

210 It is important to mention that assessing the performance of STIC-TI LE and H with respect to
211 other SEB models is not within the scope of the present study. The prime focus of the current study
212 is to assess the sensitivity of STIC-TI, temporal variability of the retrieved SEB fluxes, and cross-
213 site validation of the individual SEB components.

214 A list of variables, their symbols and corresponding units are given in Table A1 in Appendix A.

215 **2 Study area and datasets**

216 **2.1 Study site characteristics**

217 The present study was conducted using data from nine flux tower sites~~The present study was~~
218 ~~conducted at nine flux tower sites~~ (four sites in India; three sites in Australia; two sites in USA)
219 equipped with Eddy Covariance (EC) measurement systems. The distribution of the flux tower
220 sites considered for the present study are shown in Fig. 1 below. The sites cover a wide range of
221 climate, vegetation types, low fractional vegetation cover (f_c) of around 0.5 and have contrasting
222 aridity (Table 1). In India, a network of EC towers was set up under Indo-UK INCOMPASS
223 (INteraction of Convective Organization and Monsoon Precipitation, Atmosphere, Surface and
224 Sea) Program (Turner et al., 2019) at Jaisalmer (IND-Jai) in Rajasthan state, Nawagam (IND-Naw)
225 in Gujarat state, Samastipur (IND-Sam) in Bihar state and under Newton-Bhaba programme
226 (Morisson et al., 2019 a,b) at Dharwad (IND-Dha) in Karnataka state. The flux footprint for EC
227 towers in India varied from 500 m – 1 km (Bhat et al., 2019). In the present study, about 90% of
228 the fluxes came from an area within 500 m to 1 km from the EC tower. Therefore, the relative
229 contribution of vegetated land surface area to the fluxes is close to 90% (Schmid, 2002; Vesala et
230 al., 2008). The remaining percentage of fluxes were originated from an area beyond the flux
231 footprint.~~The fetch ratio of EC towers in India varied from 1:50 to 1:100 representing 90% of fetch~~
232 ~~area.~~ The mean annual f_c was found to vary from 0.25 to 0.52 with standard deviation (SD) ranging
233 from 0.1 to 0.16.

234 The IND-Jai site represents arid western zone over desert plains of natural grassland ecosystem.
 235 The region receives very low rainfall (100 – 300 mm) during monsoon and experiences a wide
 236 range in air temperature, high solar radiation, wind speed and high evaporative demand (Raja et
 237 al., 2015). The IND-Naw site represents semi-arid agroecosystem in the middle Gujarat agro-
 238 climatic zone of north-west India and has a pre-dominant rice-wheat cropping system. The IND-
 239 Sam site has sub-humid climate of north-west alluvial plain zone in the Indo-Gangetic Plain (IGP)
 240 situated in the eastern India and this site also follows rice-wheat crop rotation. IND-Dha represents
 241 humid sub-tropical climate of transition zone in the southern India and this site comprises of crops.

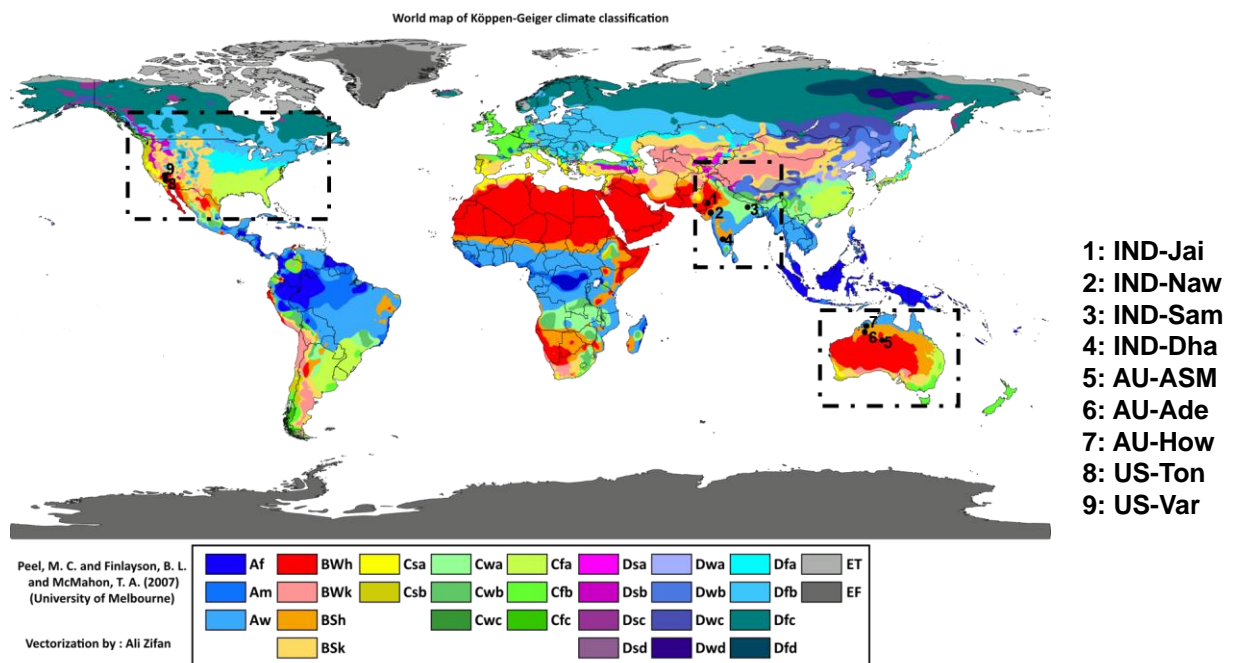


Figure 1: Locations of the flux tower sites in India, Australia and USA overlaid on climate type map. (Image Source: By Peel, M. C., Finlayson, B. L., and McMahon, T. A. (University of Melbourne) enhanced, modified, and vectorized by Ali Zifan; [Hydrology and Earth System Sciences: "Updated world map of the Köppen-Geiger climate classification".Hydrology and Earth System Sciences: "Updated world map of the Köppen-Geiger climate classification" \(Supplement\) map in PDF \(Institute for Veterinary Public Health\)](#). Legend explanation, CC BY-SA 4.0, <https://commons.wikimedia.org/w/index.php?curid=47086879>)

242 In USA, two EC tower sites were located at Tonzi Ranch (US-Ton) and Vaira Ranch (US-Var), in
 243 the lower foothills of the Sierra Nevada Mountains. Both the EC stations are part of the
 244 AMERIFLUX Management Project (<https://ameriflux.lbl.gov/>). US-Ton is classified as an oak
 245 savanna woodland, ~~on privately owned land~~. While the overstorey is dominated by blue oak trees
 246 (40% of total vegetation) with intermittent grey pine trees (3 trees ha⁻¹), the understory species

247 include a variety of grasses and herbs. The mean annual rainfall at this site is 559 mm. US-Var is
248 a grassland dominated site and the growing season is confined to the wet season only, typically
249 from October to early May. The mean annual rainfall at this site is 559 mm. The mean annual f_c
250 was found to vary from 0.18 to 0.26 and SD of the order of 0.06 to 0.07.

251 In Australia, three EC tower sites were located at Howard Springs (AU-How), Alice Springs
252 Mulga (AU-ASM), Adelaide river (AU-Ade) in the Northern Territory as part of the OzFlux
253 network (Beringer et al., 2016) and the Terrestrial Ecosystem Research Network (TERN), which
254 is supported by the National Collaborative Infrastructure Strategy (NCRIS)
255 (<http://www.ozflux.org.au/monitoringsites/index.html>). The AU-How is situated in the Black
256 Jungle Conservation Reserve representing an open woodland savanna and the mean annual rainfall
257 is 1750 mm. The AU-ASM is located on Pine Hill cattle station near Alice Springs. The woodland
258 is characterized by mulga canopy and mean annual rainfall is 306 mm. AU-Ade represents savanna
259 with a mean annual rainfall of 1730 mm. The mean annual f_c varied from 0.21 to 0.48 having SD
260 range of 0.08 - 0.17. A description of Australian flux sites is given in Beringer et al. (2016).
261 Average heights of vegetation are 1.15 m at IND-Naw, 1 m at IND-Jai, 1.23 m at IND-Sam, 1.5
262 m at IND-Dha, 6.5 m at AU-ASM, 15m at AU-How, 7 m at AU-Ade, 10 m at US-Ton, and ≤ 0.5
263 m at US-Var.~~A description of Australian flux sites is given in Beringer et al. (2016).~~

264
265
266
267
268
269
270
271
272
273
274
275
276
277

278 **Table 1:** An overview of the EC flux tower site characteristics in the present study

Hemisphere	Sites	Latitude (°N), Longitude (°E)	Climate & Vegetation	Mean f_c (SD)	Soil texture	T _A range (°C)	Mean Annual P (mm)	Observation period
Northern	Jaisalmer (IND-Jai)	26.99, 71.34	Arid grassland	0.25(±0.1)	Loamy fine sand to coarse sand	8 – 40	250	2017 – 2018
	Nawagam (IND-Naw)	22.80, 72.57	Semi-arid cropland	0.41(±0.13)	Sandy loam	9 – 39	700	2017 – 2018
	Samastipur (IND-Sam)	26.00, 85.67	Humid subtropical cropland	0.52(±0.16)	Sandy loam to loam	10 – 39	1000	2017 – 2018
	Dharwad (IND-Dha)	15.50, 74.99	Tropical Savanna	0.36(±0.11)	Shallow to medium black clay and red sandy loam soils	12 – 40	650	2016 – 2018
	Tonzi ranch (US-Ton)	38.43, -120.96	Woody Savanna	0.18(±0.06)	Red sandy clay loam	0 – 40	559	2011 – 2019
	Vaira ranch (US-Var)	38.41, -120.95	Arid grassland	0.26(±0.07)	Rocky silt loam	0 – 40	559	2011 – 2019
Southern	Alice Springs Mulga (AU-ASM)	-22.28, 133.24	Semi-arid mulga	0.21(±0.09)	Loamy sand	(-4) – 40	305	2011 – 2014
	Howard Springs (AU-How)	-12.49, 131.15	Tropical savanna	0.48(±0.17)	Red kandasol	19 – 34	1700	2011 – 2014
	Adelaide River (AU-Ade)	-13.07, 131.11	Savanna	0.42(±0.08)	Yellow hydrosol, shallow, loamy sand with coarse gravel	16 – 37	1730	2007 – 2009

279 T_A: Air temperature during the observation period; P: rainfall (mm) measured using rain gauge at flux tower site during the study
 280 period. IND is for India, AU is for Australia, and US is for the United States; SD is standard deviation of annual mean f_c which is
 281 computed from NDVI as mentioned in section 3.1.

282

283 2.2 Datasets

284 2.2.1 Micrometeorological data at flux tower sites

285 Standardized, controlled and harmonized surface energy balance (SEB) flux and meteorological
286 data from nine EC towers were used in the present analysis. In Australia, H and LE were measured
287 through the EC systems and R_N were measured through net radiometers~~the SEB measurements~~
288 ~~were carried out~~ at varying heights of 15 m, 23 m and 11.6 m at AU-Ade, AU-How and AU-ASM,
289 respectively. In India, the EC measurement height was maintained approximately at 8 m above the
290 surface, except at IND-Dha where it was installed at a height of 4.2 m. In USA, the SEB
291 measurements were carried out at tower heights of 23 m at US-Ton and 2 m US-Var. A summary
292 of the instrumentation is given in Table A2 of appendix A. All the flux tower sites were equipped
293 with a range of meteorological instrumentation which measured diurnal air temperature (T_A) and
294 relative humidity (R_H), four components of the net radiation (R_N , consisting of down- and up-
295 welling shortwave and long-wave radiation ($SW\downarrow$, $SW\uparrow$, $LW\uparrow$ and $LW\downarrow$, respectively)) above the
296 vegetated canopy. In addition, the diurnal soil heat flux (G) and soil temperature (T_{ST}) were
297 measured at all the three Australian sites and two US sites. In India, the diurnal soil heat flux was
298 measured only at IND-Dha.

299 For the Indian sites, the raw EC measurements of the turbulent wind vectors (u , v and w , for
300 horizontal, meridional and vertical, respectively), sonic temperature (T), and CO_2 and water vapor
301 mass density were recorded at a sampling rate of 20 Hz. Raw EC data were post-processed to
302 obtain level-3 quality controlled and harmonized surface fluxes at 30-minute flux averaging
303 intervals using EddyPRO® Flux Calculation Software (LI-COR Biosciences, Lincoln, Nebraska,
304 USA) using the data handling protocol described by Bhat et al. (2019). The EC data from the
305 OzFlux sites was averaged over 30 minutes recorded by the logger and processed through levels
306 using the PyFluxPro standard software processing scripts as mentioned in Isaac et al. (2017). The
307 Level 3 (L3) used in this paper was produced using PyFluxPro (Isaac et al., 2017) employing the
308 Dynamic INtegrated Gap filling and partitioning for Ozflux (DINGO) system as described in
309 Donohue et al. (2014) and Beringer et al. (2016). The quality checked EC data at 30 minute
310 intervals for two AMERIFLUX sites US-Ton and US-Var was acquired from
311 <https://doi.org/10.17190/AMF/1245971> & <https://doi.org/10.17190/AMF/1245984>, respectively.

312 **2.2.2 Remote sensing data**

313 Optical and thermal remote sensing observations available from Moderate Resolution Imaging
 314 Spectroradiometer (MODIS) (Didan et al., 2015) on-board Aqua platform were used in the present
 315 analysis (Table 2) for estimating G and associated SEB fluxes. These include eight-day land
 316 surface temperature (LST or T_s) at 1:30 pm and 1:30 am, and surface emissivity (ϵ_s) (MYD11A2),
 317 daily surface albedo (α_R) (MCD43A3), 16-day NDVI (MYD13A2). The overpass times of MODIS
 318 Aqua are at 1:30 pm and 1:30 am. The 8-day average values of clear-sky T_s available from
 319 MYD11A2 data were used (Source: <https://vip.arizona.edu/documents/viplab/MYD11A2.pdf>) for
 320 all nine flux tower sites. Since MYD21A2 LST product is known to provide better accuracy (1 –
 321 1.5 K) (Hulley et al, 2016) as compared to MYD11A2 LST over semi-arid and arid ecosystems,
 322 the former was also used in STIC-TI to compare LE and H estimates (see Table 5 in section 4.4)
 323 with the estimates of MYD11A2 LST over the arid and semi-arid sites (IND-Jai, IND-Naw, US-
 324 Ton). These include land surface products (eight-day) of noon-night land surface temperature (LST
 325 or T_s) and surface emissivity (ϵ_s) (MYD11A2), daily surface albedo (α_R) (MCD43A3), 16 day
 326 NDVI (MYD13A2). The overpass times of MODIS Aqua are at 1:30 pm and 1:30 am (IST). The
 327 noon-night pair of thermal remote sensing observations from Aqua are close to time of occurrences
 328 of maximum and minimum soil surface temperature (see Figure 2) and are therefore ideal for soil
 329 heat flux modeling using thermal inertia. The MODIS Terra overpass times are at 11 AM and 11
 330 PM and are quite away from time of occurrences of minimum-maximum soil temperatures.
 331 Therefore, MODIS Aqua acquisition times were used.

332 **Table 2:** A summary of MODIS Aqua optical and thermal remote sensing products used in the
 333 present study

Data type	Product ID (version)	Variables used	Spatial resolution (m)	Temporal resolution	Purpose	Inputs to equation numbers
Land surface temperature LST and emissivity	MYD11A2 (V006) MYD21A2 MYD11A2 (V006)	T_s (1:30 pm and am) and ϵ_s and ϵ_s	923	8-day	For estimating R_{Ni} , G_i , LE_i , H_i	(5), (13), (C6), (C7), (B8)

Surface albedo	MCD43A3 (V006)	α_R	462	8-day composite from daily	For estimating R_{Ni}, G_i	(5), (B3)
Vegetation index	MYD13Q1 (V006)	NDVI	250	16-day	For estimating G_i	(4)

334 The key variables of SEB modeling such as LST and ϵ_s , were retrieved at 923m spatial resolution
335 from MODIS Aqua noon-night thermal infrared (TIR) observations (MYD11A2) in bands 11.03
336 μm and 12.02 μm using a generalized split-window algorithm by Wan et al., (2015). The land
337 surface emissivity was estimated from land cover types, atmospheric column water vapor and
338 lower boundary air surface temperature that are separated into tractable sub-ranges for optimal
339 retrieval. The albedo was estimated from MODIS (MCD43A2 Version 6) Bidirectional
340 Reflectance Distribution Function and Albedo (BRDF/Albedo) daily dataset (Schaaf et al., (2002))
341 at 462 m spatial resolution. Eight-day compositing for albedo was done from daily products
342 (MYD11A2). NDVI was estimated from MODIS Vegetation Indices (MYD13Q1) Version 6 data
343 and are generated every 16-day at 250 meter (m) spatial resolution as a Level 3 product.
344 MYD13Q1 contains Normalized Difference Vegetation Index (NDVI) and Enhanced Vegetation
345 Index (EVI). In the present study, NDVI has been used because of its universal applicability (Xue
346 and Su, 2017; Drori et al. 2020; Bhandari et al., 2012). All the input remote sensing variables
347 mentioned in table 2 are resampled to spatial resolution of MYD11A2 (V006) product (923 m).

348 **3 Methodology**

349 **3.1 Coupled soil heat flux-SEB model**

350 In this paper, we modified a thermal inertia (TI) based soil heat flux (G) model using noon-night
351 thermal remote sensing observations and thereafter coupled the TI-based G with STIC1.2. A clear-
352 sky net radiation (R_N) model was also introduced into this coupled model and R_N estimation
353 algorithm is described in Appendix B. The estimation of G through modifying MV2007-TI
354 approach and its coupling with STIC1.2 is the most novel component of the modeling scheme, and
355 it is therefore described in the main body of the paper (section 3.1.1). Such a coupling enabled the
356 implementation of a mechanistic G model along with an analytical SEB model using optical-

357 thermal remote sensing data. The coupled model is hereafter referred as STIC-TI. The noteworthy
 358 features of STIC-TI are: (1) estimating G by modifying the mechanistic MV2007-TI model using
 359 noon-night T_s data from thermal remote sensing observations available through polar orbiting
 360 satellite platform (e.g. MODIS Aqua), (2) coupling MV2007-TI G model with STIC1.2 to
 361 simultaneously estimate surface moisture availability (M), G, and SEB fluxes, (3) introducing
 362 moisture availability information in G to better constrain the aerodynamic and canopy-surface
 363 conductances as well as the SEB fluxes, (4) the G model uses fundamental soil physical properties,
 364 moisture constants and soil texture that majorly influence soil heat conduction, (5) derivation of
 365 amplitude of ecosystem-scale surface soil temperature (from top soil to 0.1 m soil depth).

366 3.1.1 MV2007 soil heat flux model based on Thermal Inertia (TI)

367 The functional form for estimating instantaneous G (G_i , hereafter) (eq. 2 below) is based on the
 368 harmonic analysis of soil surface temperature and is described in detail by Murray and Verhoef
 369 (2007) and Maltese et al. (2013).

$$G_i = \Gamma \left[(1 - 0.5f_C) \left(\sum_{n=1}^k A \sqrt{n\omega} \sin \left(n\omega t + \phi'_n + \frac{\pi}{4} - \frac{\pi\Delta t}{12} \right) \right) \right] = \Gamma J_s \quad (2)$$

370 G_i is the soil heat flux at the surface at a particular instance (W m^{-2}), Γ is the soil thermal inertia
 371 ($\text{J m}^{-2} \text{K}^{-1} \text{s}^{-0.5}$), k is the total number of harmonics used, A is the amplitude ($^{\circ}\text{C}$) of the n^{th} soil
 372 surface temperature (T_{ST}) harmonic, ω is the angular frequency (rads^{-1}), t is the time (s), ϕ'_n is the
 373 phase shift of the n^{th} soil surface temperature harmonic (rad), J_s is the summation of harmonic
 374 terms of soil surface temperature (K), and Δt (s) is time offset between the canopy composite
 375 temperature and the below-canopy soil surface temperature. Here, we represent G_i and A as
 376 ecosystem-scale ($\leq 1\text{km}$) soil heat flux and surface soil temperature amplitude (averaged from soil
 377 surface to 10 cm depth)(~~within 0.1 m from the soil top~~), respectively and assume it to be valid for
 378 different vegetated landscape.

379 Since we have considered a single pair (noon-night corresponding to 1:30 pm and 1:30 am) of
 380 MODIS aqua LST data in the present study, the phase shift (ϕ'_n) is taken as zero and number of
 381 harmonics is taken as one ($k=1$) for estimating G_i .~~Since we have considered a single pair (noon-~~

382 ~~night corresponding to 1 pm and 1 am) of MODIS aqua LST data in the present study, the phase~~
 383 ~~shift (ϕ'_n) is taken as zero and number of harmonics is taken as one ($k=1$) for estimating noontime~~
 384 ~~G_i . Thus equation (2) is modified as follows:~~

$$G_i = \Gamma \left[(1 - 0.5f_c) \left(A\sqrt{\omega} \sin \left(\omega t' + \frac{\pi}{4} - \frac{\pi \Delta t}{12} \right) \right) \right] = \Gamma J_s \quad (3)$$

385 Δt (s) is found to be 1.5 h (Murray and Verhoef, 2007). With the two boundary values (i.e., $\Delta t=1.5$
 386 h for $f_c = 1$ and $\Delta t = 0$ for $f_c = 0$), a linear approach is proposed here to describe the time offset Δt
 387 as a function of vegetation fraction (f_c) (Murray and Verhoef, 2007; Maltese et al., 2013). The f_c
 388 was derived from NDVI on a given day or period and its practically occurring upper-lower limits
 389 obtained from annual cycle.

390
 391

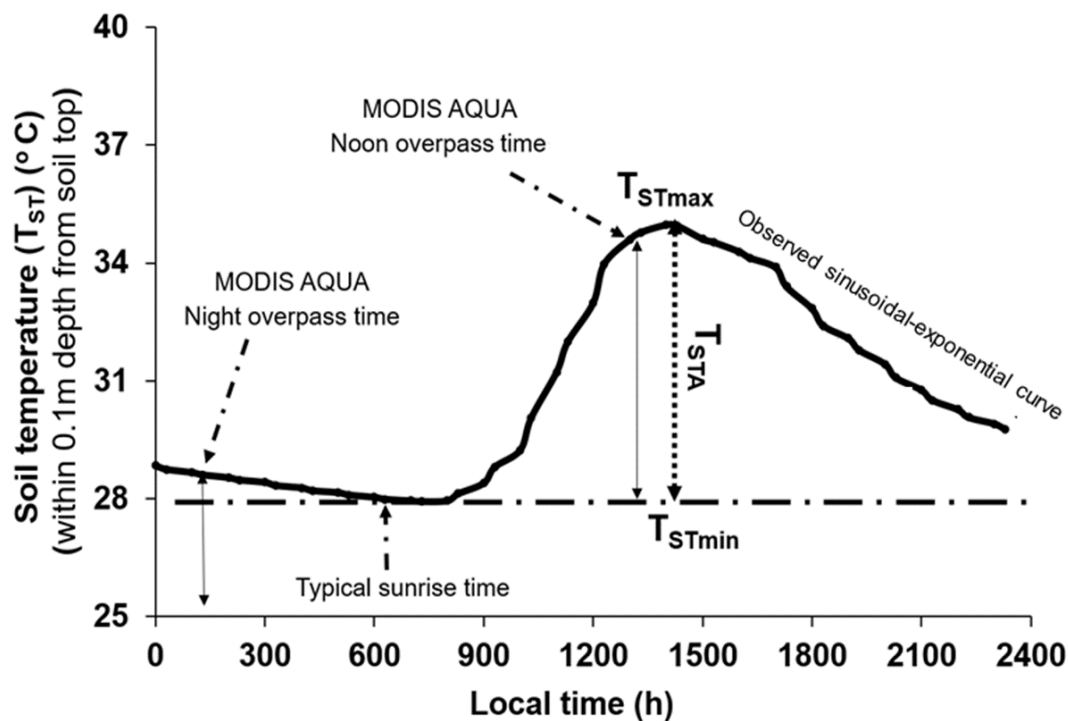
$$\Delta t = 1.5 f_c \quad (4)$$

392 **3.1.1.1 Scaling function for estimating ecosystem-scale surface soil temperature amplitude (A)**

393 Estimating ecosystem-scale A involves two steps, (a) computing point-scale soil surface
 394 temperature amplitude (from surface to 0.1m depth) (T_{STA} , hereafter) from the available
 395 measurements of soil surface temperature, and (b) linking T_{STA} with remote sensing variables to
 396 develop scaling functions for A. Point-scale soil temperature measured at different depths within
 397 top 10 cm soil layer at AU-ASM, US-Ton, US-Var was averaged and considered as representative
 398 surface soil temperature (0 – 10 cm). For Ind-Dha and AU-Ade, single-depth (10 cm) soil
 399 temperature measurement was used. Studies also showed that LST carries some signal beneath the
 400 skin of the surface (Johnston et al., 2022).

401 Several studies suggested theoretical sinusoidal trajectory of soil surface and sub-surface
 402 temperatures (Gao et al., 2010), where the amplitude is maximum at the surface, and it gradually
 403 decreases with depth to become 37% of surface amplitude until the damping depth (Hillel, 1982).
 404 However, at deeper depths, soil temperatures remain constant with time and do not show many
 405 fluctuations as compared to surface or near-surface soil temperatures. This invariant soil
 406 temperature is called deep soil temperature (Mihailovic et al., 1999).where the amplitude is

407 ~~maximum at the surface and it gradually decreases with depth to become close to zero until the~~
 408 ~~damping depth where soil temperature is almost invariant through day-night called deep soil~~
 409 ~~temperature.~~ However, the diurnal surface soil temperature measurements (within top 0.1 m depth)
 410 across different flux tower sites showed a sinusoidal-exponential behavior, i.e. sinusoidal pattern
 411 from sunrise until the afternoon and exponential pattern from afternoon through sunset to the next
 412 sunrise. An illustrative example of the theoretical and observed trajectories of surface soil
 413 temperature is shown in Fig. 2. This diurnal surface soil temperature variation has a single
 414 harmonic component (Gao et al., 2010). For computing T_{STA} , theoretical half-curve of sinusoidal
 415 pattern is assumed and was derived from measurements as exemplified in Fig 2.
 416



417 **Figure 2.** An illustrative example of typical diurnal variation of observed soil temperature (T_{ST})
 (from surface to 0.1m depth) at OzFlux sites and timings of MODIS AQUA observations. Here,
 T_{STmax} and T_{STmin} are maximum and minimum point-scale observed soil surface temperatures

418 It is evident from Fig. 2 that T_{STmin} represents minimum surface soil temperature occurring 1-1.5h
 419 after sunrise and T_{STmax} occurs during 12.30 – 15.00h local time. The *in-situ* measured T_{ST} on
 420 completely clear-sky days at OzFlux sites were used to extract T_{STmax} and T_{STmin} and T_{STA} was
 421 derived as $(T_{STmax} - T_{STmin})$ from the theoretical half-curve of sinusoidal pattern.

422 ~~It is evident from Fig. 2 that T_{STmin} represents minimum surface soil temperature occurring 1–1.5~~
 423 ~~h after sunrise and T_{STmax} occurs during 12.30–15.00 h local time. T_{STmin} is thus close to deep soil~~
 424 ~~temperature as well as minimum soil temperature of other sub-surface soil layers. Both T_{STmin} and~~
 425 ~~T_{STmax} represent lower and upper limits of surface soil temperature on a given day and also lower~~
 426 ~~and upper boundary conditions of soil heat flux conducting through topsoil at noontime. The *in-*~~
 427 ~~*situ* measured T_{ST} on completely clear sky days at OzFlux sites were used to extract T_{STmax} and~~
 428 ~~T_{STmin} . The T_{STA} was derived as the difference between T_{STmax} and T_{STmin} from the theoretical half-~~
 429 ~~curve of sinusoidal pattern.~~

430 T_{STA} is generally influenced by several land surface characteristics such as surface temperature
 431 and surface albedo of soil-canopy complex, surface heat capacities, fractional canopy cover and
 432 thermal conductivity (White, 2013). T_S and α_R are the major thermal and reflective land surface
 433 properties that have strong synergy with surface soil temperature dynamics. Hence, we have used
 434 bivariate regression analysis to develop a scaling function for estimating ecosystem-scale T_{STA}
 435 (top to 0.1m depth). The bivariate regression is based on the difference of noon (d) and night (n)
 436 T_S data and α_R (Duan et al., 2013, Li Tian et al., 2014) from MODIS Aqua. The scaling function
 437 given in eq. (5) estimates ecosystem-scale T_{STA} (symbolized as ‘A’ in equation 5) from surface to
 438 0.1 m soil depth:

$$A = B_1(T_{Sd} - T_{Sn}) + B_2(\alpha_R) + B_3 \quad (5)$$

439 Here, B_1 , B_2 , B_3 are coefficients of regression model; T_{Sd} and T_{Sn} are noon and nighttime LST,
 440 respectively. The results of this regression analysis are elaborated in section 4.1.

441 3.1.1.2 Estimating Γ

442 Γ is the key variable for estimating G_i using eq. (2). MV2007 adopted the concept of normalized
 443 thermal conductivity (Johansen, 1975) and developed a physical method to estimate Γ as follows:

$$\Gamma = e^{[Y'(1 - S_r^{(Y' - \delta)})]}(\tau_* - \tau_0) + \tau_0 \quad (6)$$

444 where τ_* and τ_0 are the thermal inertia for saturated and air-dry soil ($J m^{-2} K^{-1} s^{-0.5}$); $\tau_0 = D_1\theta^* + D_2$;
 445 $\tau_* = D_3(\theta^{*-1.29})$; $Y'(-)$ is a parameter depending on the soil texture (Murray and Verhoef, 2007;
 446 Minasny, 2007; Anderson et al., 2007); $S_r(m^3 m^{-3})$ is relative saturation and is equal to (θ/θ^*) ; δ

447 (unitless) is the shape parameter which is dependent on the soil texture. θ^* ($\text{m}^3 \text{m}^{-3}$) is the soil
 448 porosity (equal to the saturated soil moisture content when soil moisture suction is zero), θ (cm^3
 449 cm^{-3}) is the volumetric soil moisture and D_1 , D_2 , D_3 are coefficients which were derived from a
 450 large number of experimental data. The reported global values of D_1 , D_2 , and D_3 were taken as -
 451 1062.4, 1010.8, 788.2, respectively (Maltese et al., 2013). The value for θ^* and shape parameter
 452 for soil textures across study sites were specified according to Van Genuchten et al. (1980). The
 453 details are mentioned in Table E1 of Appendix E.

454 In the present study, the relative soil moisture saturation, S_r (θ/θ^*) is represented in terms of an
 455 aggregated moisture availability (M) of canopy-soil complex through a linear function (eq. 12). In
 456 case of zero canopy cover, M represents the soil moisture availability from surface to 0.1 m depth.
 457 In sparse and open canopy, rates of moisture availability from soil to root and root to canopy were
 458 assumed same.

459 Theoretically, M is expressed as available soil moisture fraction between field capacity (θ_{fc}) and
 460 permanent wilting (θ_{wp}) point as given in eq. (7) below.

$$M = \frac{\theta - \theta_{wp}}{\theta_{fc} - \theta_{wp}} \quad (7)$$

461 Where, θ_{fc} ($\text{m}^3 \text{m}^{-3}$) is the volumetric soil moisture at the field capacity (at a suction of 330 hPa)
 462 and θ_{wp} ($\text{m}^3 \text{m}^{-3}$) is the volumetric soil moisture at the permanent wilting point (at suction of 15000
 463 hPa) (Singh, 2007). Since θ_{fc} , θ^* , θ_{wp} are characteristic volumetric soil moisture contents
 464 corresponding to specific suctions~~Where, θ_{fc} ($\text{m}^3 \text{m}^{-3}$) is the volumetric soil moisture at the field~~
 465 ~~capacity (at a suction of 330 hpa) and θ_{wp} ($\text{m}^3 \text{m}^{-3}$) is the volumetric soil moisture at the permanent~~
 466 ~~wilting point (at suction of 15000 hpa) (Singh, 2007). Since θ_{fc} , θ^* , θ_{wp} are soil moisture constants~~
 467 and depends on the soil texture, dividing the numerator and denominator in eq. (7) by θ^* gives the
 468 following expression:

$$M = \frac{\frac{\theta}{\theta^*} - \frac{\theta_{wp}}{\theta^*}}{\frac{\theta_{fc}}{\theta^*} - \frac{\theta_{wp}}{\theta^*}} \quad (8)$$

469 Due to their dependence on soil texture, the ratios (θ_{fc}/θ_*) and (θ_{wp}/θ_*) are treated as constants.
 470 These are represented as C and C' in the later equations (eq. 9, 10, and 11). The constants, C and
 471 C' vary from 0.3 to 0.8 and from 0.1 to 0.4 (Murray and Verhoef, 2007; Minasny et al., 2011;
 472 Anderson et al., 2007), respectively over different soil textures.

$$M = \frac{\frac{\theta}{\theta_*} - C'}{C - C'} \quad (9)$$

$$M(C - C') = \left(\frac{\theta}{\theta_*}\right) - C' \quad (10)$$

473 By replacing S_r in eq. (6) as θ/θ_* and by rearranging eq. (10), the following linear function is
 474 obtained.

$$S_r = \frac{\theta}{\theta_*} = M(C - C') + C' = M' \quad (11)$$

475 Thus, the modified equation to calculate Γ is given by eq. (12) as follows:

$$\Gamma = e^{[Y'(1 - M'(\alpha' - \delta))]}(\tau_* - \tau_0) + \tau_0 \quad (12)$$

476 By substituting the values obtained from eq. (4), (5) and (12) into eq. (3), we obtained the
 477 instantaneous ecosystem-scale G_i corresponding to MODIS Aqua noontime overpass. The intrinsic
 478 link between G_i estimates through MV2007-TI and SEB scheme in STIC1.2 is made through M ,
 479 where the computation of M follows the procedure as described in Mallick et al. (2016, 2018a, b)
 480 and Bhattarai et al. (2018). (description in Appendix C).

481 **3.1.1.3 Estimating M**

482 In STIC1.2, an aggregated moisture availability (M) of canopy-soil complex is expressed as the
 483 ratio of the ‘vapor pressure difference’ between the aerodynamic roughness height of the canopy
 484 (i.e., source/sink height) and air to the ‘vapor pressure deficit’ between aerodynamic roughness
 485 height to the atmosphere:

$$M = \frac{(e_0 - e_A)}{(e_0^* - e_A)} = \frac{(e_0 - e_A)}{\kappa(e_S^* - e_A)} = \frac{s_1(T_{0D} - T_D)}{\kappa s_2(T_S - T_D)} \quad (13)$$

486 Where e_0 and e_0^* are the actual and saturation vapor pressure at the source/sink height; e_A is the
 487 atmospheric vapor pressure; e_S^* is the saturation vapor pressure at the surface; T_{0D} is dew point
 488 temperature at the source/sink height; T_S is the LST; T_D is the air dew point temperature; s_1 and s_2
 489 are the psychrometric slopes of the saturation vapor pressure and temperature between $(T_{0D} - T_D)$
 490 versus $(e_0 - e_A)$ and $(T_S - T_D)$ versus $(e_S^* - e_A)$ relationship; and κ is the ratio between $(e_0^* - e_A)$
 491 and $(e_S^* - e_A)$. To solve the eq. (13), estimation of T_{0D} is necessary. An initial estimate of T_{0D} [T_{0D}
 492 = $[(e_S^* - e_A) - s_3 T_S + s_1 T_D]/(s_1 - s_3)$] and M were obtained following Venturini et al. (2008) where
 493 s_1 and s_3 were approximated in T_D and T_S , respectively. However, eq. (13) cannot be directly
 494 solved because there are two unknowns in one equation. However, since T_{0D} also depends on LE
 495 (Mallick et al., 2016, 2018a), an iterative updation of T_{0D} (and M) was carried out by expressing
 496 T_{0D} as a function of LE [$T_{0D} = T_D + (\gamma LE / \rho c_p g_{AS1})$] which is described in detail by Mallick et al.
 497 (2016, 2018a) and Bhattarai et al. (2018). In the numerical iteration, s_1 was not updated to avoid
 498 numerical instability and it was expressed as a function of T_D .

499 3.1.2 STIC-TI: Coupling modified MV2007-TI and STIC 1.2

500 The initiation of the coupling between MV2007-TI and STIC1.2 was executed through linking G_i
 501 estimates from the modified MV2007-TI with M estimates from STIC1.2. Having the initial
 502 estimates of M (through eq. 13), an initial estimation of G_i was made from eq. (2) where S_r in eq.
 503 11 was replaced with the initial estimates of M' . From the initial estimates of G_i (eq. 2) and R_{Ni}
 504 (equations in Appendix B), initial estimates of LE_i and H_i were obtained through the PMEB
 505 equation. Analytical expressions of the conductances for estimating H and LE through the PMEB
 506 equation were obtained by solving the state equations as described in the Appendix. Given the
 507 initial estimates of G_i (eq. 2) and R_{Ni} (equations in Appendix B), initial estimation of the
 508 conductances, LE_i and H_i were obtained. The process was then iterated by updating T_{0D} [$T_{0D} = T_D$
 509 + $(\gamma LE / \rho c_p g_{AS1})$] and M in every time step (as mentioned in Mallick et al., 2016, 2018a), and re-
 510 estimating G_i (using eq. 3), net available energy ($R_{Ni} - G_i$), conductances, LE_i and H_i , until stable
 511 estimates of LE_i were obtained. The conceptual block diagram and algorithm flow of STIC-TI is
 512 shown in Fig. 3a and Fig 3b, respectively.

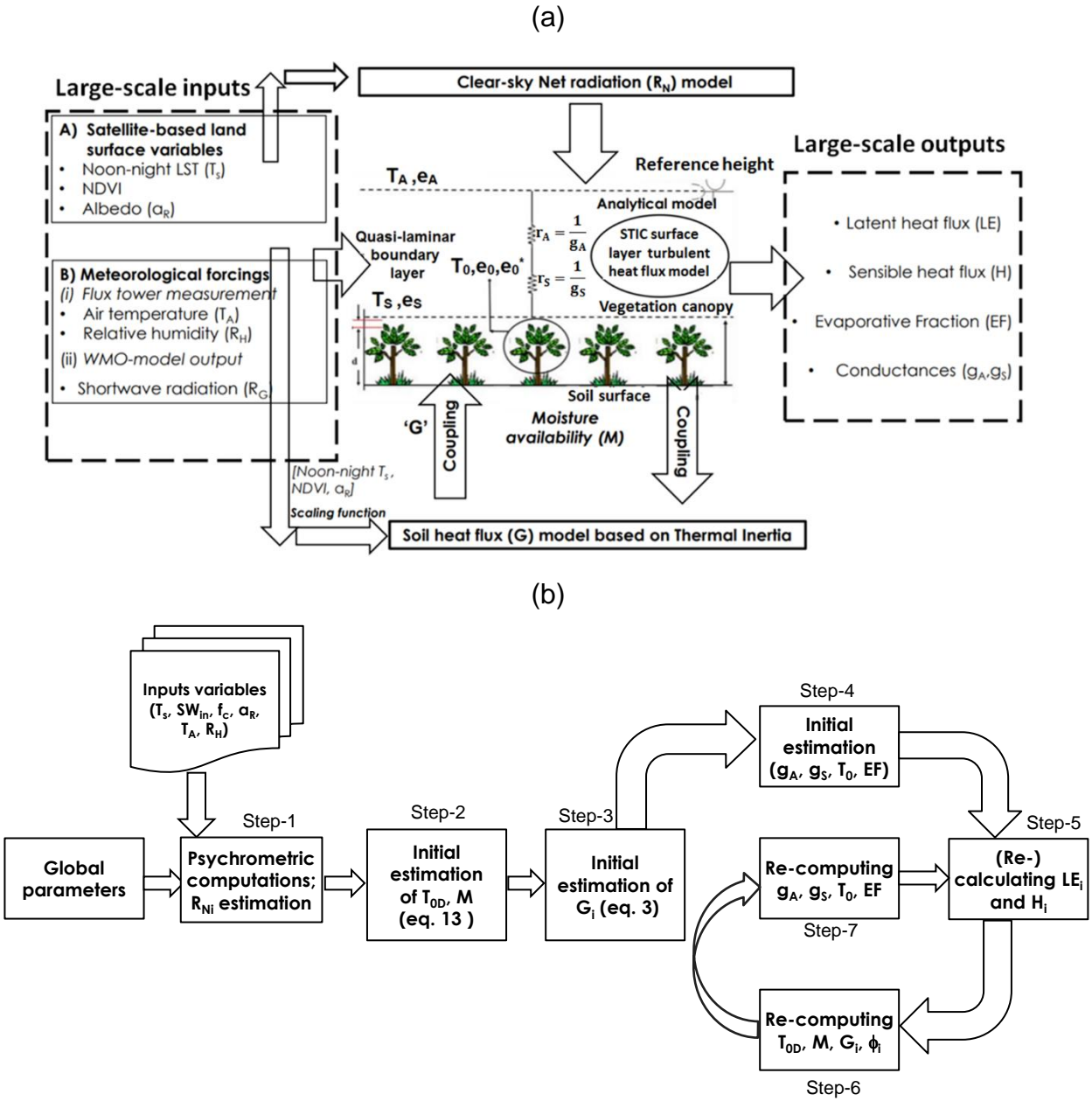


Figure 3: (a) Conceptual diagram of STIC-TI model showing different input variables and model outputs; (b) Algorithmic flow for estimating G and associated SEB fluxes through STIC-TI.

513 Examples of iterative stabilization of G_i and LE_i for Indian, Australian and US ecosystems of India
 514 are shown in Fig. 4. The iterative stabilization of G_i and LE_i was obtained between 8-25 iterations
 515 for all sites.

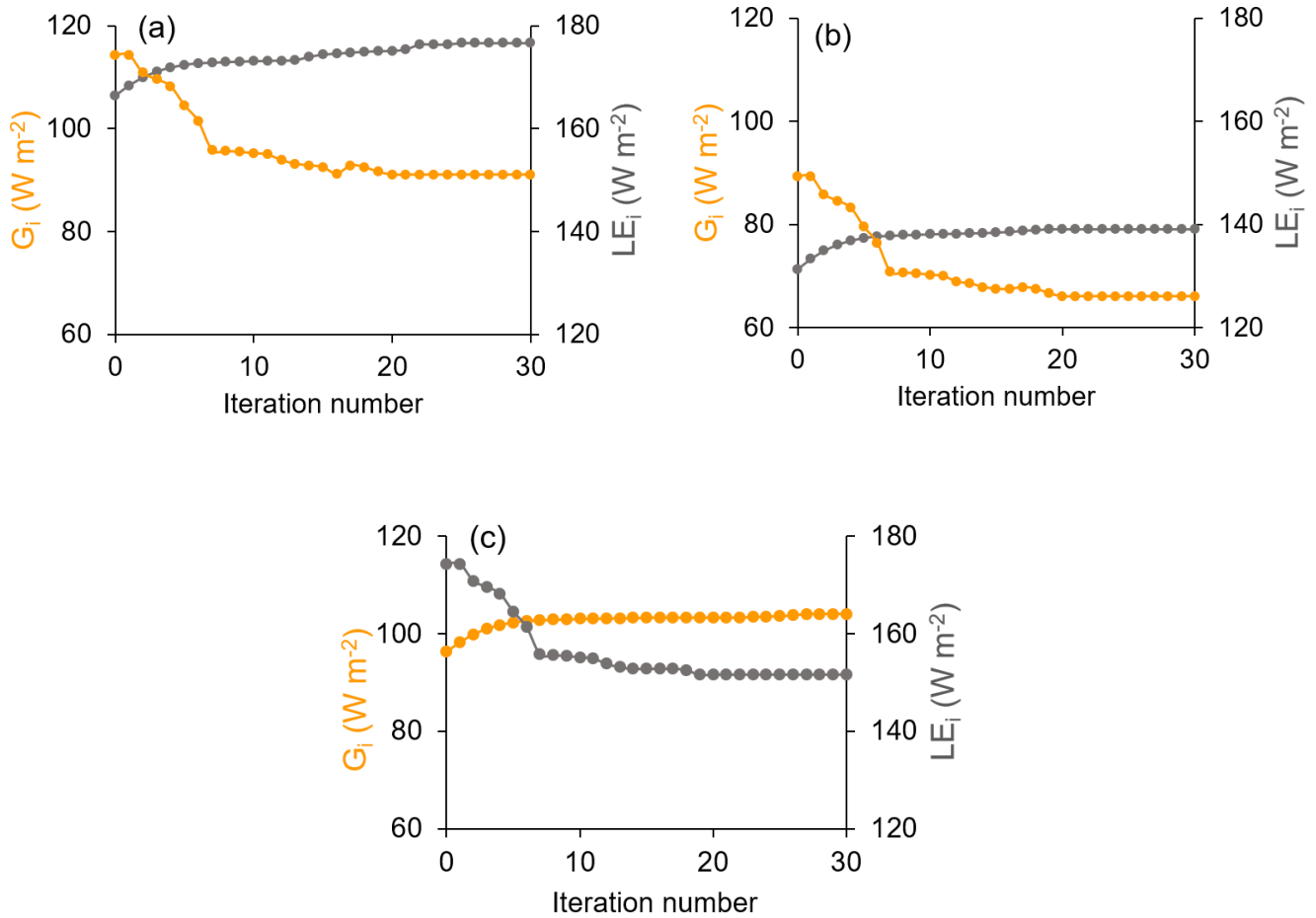


Figure 4: Illustrative examples of iterative stabilization of STIC-TI G_i (yellow marker line) and LE_i (grey marker line) in (a) IND-Jai, (b) AU-ASM, (c) US-Ton

516 The noteworthy features of STIC-TI are: (1) estimating G by modifying the mechanistic MV2007-
 517 TI model using noon and midnight T_s information from thermal remote sensing observations
 518 available through polar orbiting satellite platform (e.g. MODIS Aqua), (2) coupling the
 519 mechanistic MV2007-TI G model with STIC1.2 to simultaneously estimate surface moisture
 520 availability (M), G , and SEB fluxes, (3) introducing water stress information in G (through M) to
 521 better constrain the aerodynamic and canopy-surface conductances as well as the SEB fluxes, and
 522 (4) derivation of amplitude of ecosystem-scale surface soil temperature (from top soil to 0.1 m soil
 523 depth).

524 3.1.3 Generation of remote sensing inputs

525 Two of the key variables in SEB modeling are T_s and ϵ_s . These two variables were retrieved at
 526 923m spatial resolution from MODIS Aqua noon-night TIR observations (MYD11A2) in bands

527 11.03 μm and 12.02 μm using a generalized split-window algorithm (Wan et al., 2015). For
528 optimal retrieval, tractable sub-ranges of atmospheric column water vapor and lower boundary air
529 surface temperature were used. Land surface emissivity was estimated from land cover types and
530 anisotropy factors. The MYD21A2 LST product was generated using Temperature-Emissivity
531 Separation (TES) algorithm (Hulley et al, 2016) and improved water vapor scaling method to
532 remove the atmospheric effects. Albedo was estimated from MODIS (MCD43A2 Version 6.0)
533 Bidirectional Reflectance Distribution Function and Albedo (BRDF/Albedo) daily dataset (Schaaf
534 et al., 2002)) at 462 m spatial resolution. Actual albedo is a value which is interpolated between
535 white-sky and black-sky albedo as a function of fractional diffuse skylight (which is a function of
536 aerosol optical depth). NDVI was obtained from level 3 MODIS vegetation indices product
537 (MYD13Q1, version 6.1), which are generated every 16-day at 250 meter (m) spatial resolution.
538 All the input remote sensing variables mentioned in table 2 were resampled to spatial resolution
539 of MYD11A2 product (923 m).

540 **3.2 Sensitivity and statistical analysis**

541 The accuracy of STIC-TI heavily depends on the accuracy of T_s , NDVI, and α_R due to the dual
542 role of T_s in estimating M and G_i , the role of NDVI in G_i , and the combined role of T_s and α_R in
543 estimating R_{Ni} . Therefore, one-dimensional sensitivity analysis was conducted to assess the
544 impacts of uncertainty in T_s , NDVI and α_R on G_i , H_i and LE_i . The sensitivity was assessed by
545 varying noon-time T_s by ± 0.5 K, $\pm 1.5-1.0$ K and ± 1.5 K (keeping nighttime T_s constant so that
546 amplitude can vary automatically); varying NDVI by ± 0.05 ; ± 0.10 , ± 0.15 ; and varying albedo by
547 ± 0.02 , ± 0.05 , ± 0.10 , respectively. SEB fluxes were computed by using T_s , NDVI, and α_R for three
548 different periods of the year in all the eight ecosystems. Sensitivity analyses were conducted by
549 increasing and decreasing systematically T_s , NDVI, α_R from its central value while keeping the
550 other variables and parameters constant. This procedure was selected because the fluxes and
551 intermediate outputs of the STIC-TI model reflect an integrated effect due to uncertainty in T_s . In
552 the first run, SEB fluxes were computed using *in-situ* T_s measurements obtained from the flux
553 tower outgoing longwave radiation measurements. Then T_s was increased and decreased at
554 constant interval and a new set of fluxes were estimated. In the similar way, α_R and NDVI were
555 increased and decreased at constant intervals and new set of fluxes were computed. The sensitivity
556 of STIC-TI was assessed by the equation 14.

$$\text{Sensitivity} = \frac{E_{i0} - E_{iM}}{O_i} * 100 \quad (14)$$

557 E_{i0} is the estimated (original) model output and E_{iM} is the estimated (modified) output obtained by
 558 changing the variable whose sensitivity is to be tested. O_i is actual measurements. Apart from the
 559 sensitivity analysis, the following set of statistical metrics were used to assess model performances.

$$R^2 = \left(\frac{\sum_{i=1}^n (E_i - \bar{E})(O_i - \bar{O})}{\sqrt{\sum_{i=1}^n (E_i - \bar{E})^2} \sqrt{\sum_{i=1}^n (O_i - \bar{O})^2}} \right)^2 \quad (15)$$

$$\text{RMSE} = \sqrt{\frac{\sum_{i=1}^n (E_i - O_i)^2}{n}} \quad (16)$$

$$\text{BIAS} = \frac{\sum_{i=1}^n (E_i - O_i)}{n} \quad (17)$$

$$\text{MAPD} = \frac{100}{n} \sum_{i=1}^n \left| \frac{E_i - O_i}{O_i} \right| \quad (18)$$

$$\text{KGE} = 1 - \sqrt{(r - 1)^2 + \left(\frac{\sigma_E}{\sigma_o} - 1 \right)^2 + \left(\frac{\bar{E}}{\bar{O}} - 1 \right)^2} \quad (19)$$

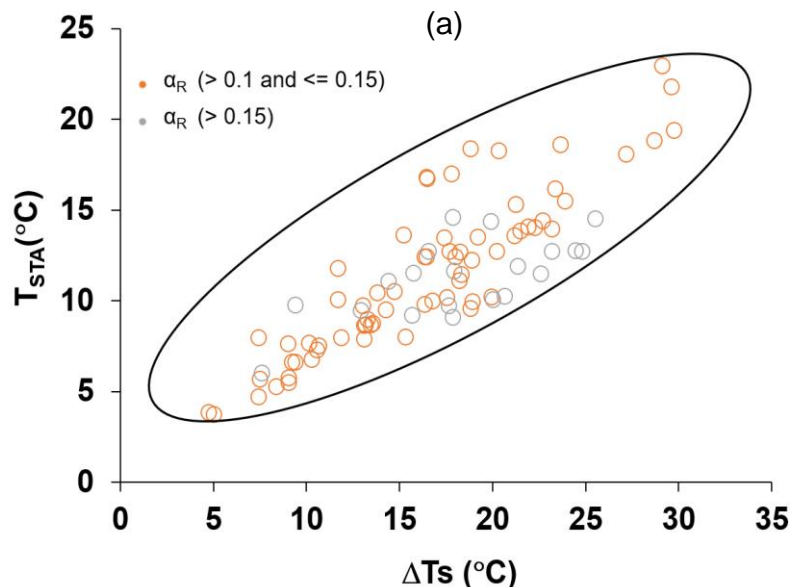
560 Where R^2 is the coefficient of determination, RMSE is root-mean-square error, BIAS is the mean
 561 bias, MAPD is the mean absolute percent deviation, KGE is Kling-Gupta efficiency, n is the total
 562 number of data pairs, the bar indicates mean value of the measured variable and model estimates
 563 of the same variable. E_i and O_i are the model estimated and measured SEB fluxes, r is the Pearson's
 564 correlation coefficient and \bar{O} is the average of measured values and \bar{E} is the average of estimated
 565 values and σ_o is standard deviation of observation values and σ_E is the standard deviation of
 566 estimated values. The KGE has been widely used for calibration and evaluation hydrological
 567 models in recent years and it combines the three components of Nash-Sutcliffe efficiency (NSE)
 568 of model errors (i.e. correlation, bias, ratio of variances or coefficients of variation) in a more
 569 balanced way. But it has not been widely used for analyzing the ET model performances. $\text{KGE} = 1$
 570 indicates perfect agreement between modelled estimates and observations. The performance of a

571 model is considered ‘poor’ for KGE between 0 and 0.5 and models with negative KGE values is
572 considered ‘not satisfactory’.

573 4 Results

574 4.1 Ecosystem- scale surface soil temperature amplitude (A)

575 The scaling functions developed to estimate ecosystem-scale (1 km) surface soil temperature
576 amplitude (A) from point-scale T_{STA} were used to estimate G_i . However, before the development
577 of the scaling functions, analysis was carried out to investigate the relationship of soil temperature
578 amplitude between the two different spatial scales. The scatterplot (Fig. 5a) of noon-night LST
579 difference (ΔT_s) versus T_{STA} for different albedo classes showed a linear increase in ΔT_s with
580 increasing T_{STA} . However, some divergence of data points within the cluster were also noticed
581 which could be associated with different albedo (α_R) levels. Bivariate linear function was fitted
582 between T_{STA} as predictand (Y) versus ΔT_s ($T_{sd} - T_{sn}$) and α_R as predictors (X1 and X2,
583 respectively). The function was found to be $Y = 0.59X_1 - 51.3X_2 + 8.66$ by combining the data
584 of nine ecosystems ($r = 0.86$). The coefficients in the above expressions correspond to B1 (0.59),
585 B2 (51.3), B3 (8.66) of eq. 5 in section 3.1.1.1. The estimated amplitude from this ecosystem-scale
586 predictors and scaling functions was treated as ecosystem-scale surface soil temperature amplitude
587 (A).



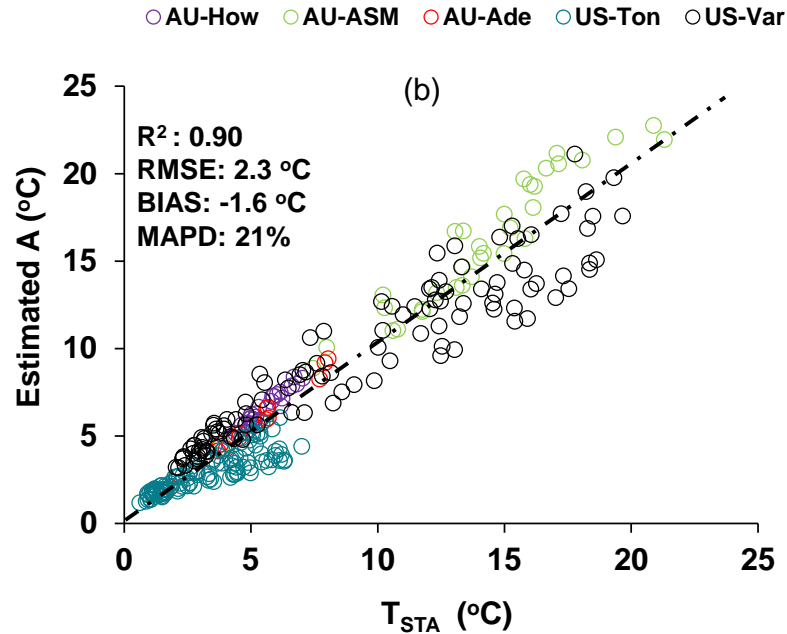


Figure 5. (a) Two-dimensional scatterplots between (ΔT_s) versus T_{STA} at different α_R levels over different ecosystems. Here T_{STA} in y-axis is the observed soil temperature amplitude that is used to develop the scaling function and delta ΔT_s is noon-night LST difference of MODIS AQUA; (b) Validation of ~~the~~ ecosystem-scale estimates of A from the above functions over different ~~ecosystems and for independent years/sites~~.

588 ~~The validation~~ Validation of the ecosystem-scale estimates of A from the above functions over
 589 different ecosystems is shown in Fig. 5b with respect to T_{STA} for the independent datasets. The
 590 estimated A was found to have MAPD of 21%, bias of -1.6°C and $R^2 = 0.90$ over different
 591 ecosystems. The temporal variation of estimated A and T_{STA} is shown in Fig D1 in Appendix D.
 592 Further analysis was carried out to investigate the bias in A at three fractional vegetation cover
 593 (fc) slabs ($fc < 0.3$; $0.3 \leq fc \leq 0.5$; $fc > 0.5$) representing bare soil (slab 1), 30 – 50% canopy cover (slab
 594 2) and more than 50% canopy cover (slab 3), respectively. While negative bias was noted for slab
 595 1 and slab 3 (-0.54°C and -0.83°C), the bias was positive (0.49°C) in the intermediate fc which
 596 represents sparse and patchy canopy cover. The signals of surface albedo, emissivity and
 597 temperatures of soil surface and canopy are relatively pure in slab1 and slab 3 as compared to slab
 598 2, where the surface signal carries more heterogeneity. Given T_{STA} is computed from the in-situ
 599 measurements, it is likely to carry more heterogeneity in slab 2 as compared to the other two slabs.
 600 The land surface emissivity in MYD11A2 was estimated from land cover types and anisotropy

601 factor, which have differential impacts on T_{ST} and T_s leading to such opposite bias in slab 2 as
602 compared to slab 1 and slab 3.

603 **4.2 Sensitivity analysis of STIC-TI G_i , LE_i and H_i to land surface variables**

604 **4.2.1 Sensitivity of G_i to land surface variables**

605 The average sensitivity of G_i to three land surface variables (T_s , NDVI, α_R) by combining the
606 estimates of wet and dry periods is shown in Fig. 6. G_i was found to be substantially sensitive to
607 T_s with error magnitude ranging from 2 – 18% due to T_s uncertainties of $\pm 0.5 - 2.5$ K (Fig. 6a),
608 with greater sensitivity to T_s during the summer season as compared to other seasons. The median
609 sensitivity of G_i due to $\pm 5 - 10\%$ uncertainty in α_R varied from 5 to 12% in all the ecosystems (Fig.
610 6b). The uncertainties in NDVI revealed 2 to 15% error in G_i estimates (Fig. 6c), and no significant
611 difference in the mean sensitivity due to NDVI uncertainties was noted between the ecosystems.
612 The sensitivity of G_i decreased with increasing values of NDVI.

613 **4.2.2 Sensitivity of LE_i and H_i to land surface variables**

614 Both LE_i and H_i were sensitive to T_s to the order of 2 – 29% (LE_i) and 5 – 35% (H_i) for T_s
615 uncertainty of $\pm 0.5 - 2.5$ K from its mean values (Table 3). Interestingly, LE_i was more sensitive
616 to T_s uncertainties as compared to H_i in the rainfed ecosystems. The highest mean sensitivity of
617 LE_i to T_s was found in arid (IND-Jai: 2 – 28%), semi-arid (AU-ASM: 5 – 21%), tropical savanna
618 (IND-Dha: 3 – 26%), savanna (US-Ton: 4-29%) and arid (US-Var: 3-26%) ecosystems. The mean
619 sensitivity of H_i to T_s was maximum in sub-humid (IND-Sam: 2 – 32%), semi-arid (IND-Naw: 2
620 – 28%), savanna (AU-Ade: 8 – 17%) (Table 3). A greater sensitivity of the SEB fluxes due to α_R
621 uncertainties was found than due to NDVI. The median sensitivity of LE_i and H_i due to 10%
622 uncertainty from mean α_R varied within 2 – 16% in all the ecosystems (Table 3). By contrast,
623 errors in the two SEB fluxes were substantially low (2 – 13%) due to $\pm 0.05 - 0.15$ uncertainty
624 from mean NDVI (Table 3).

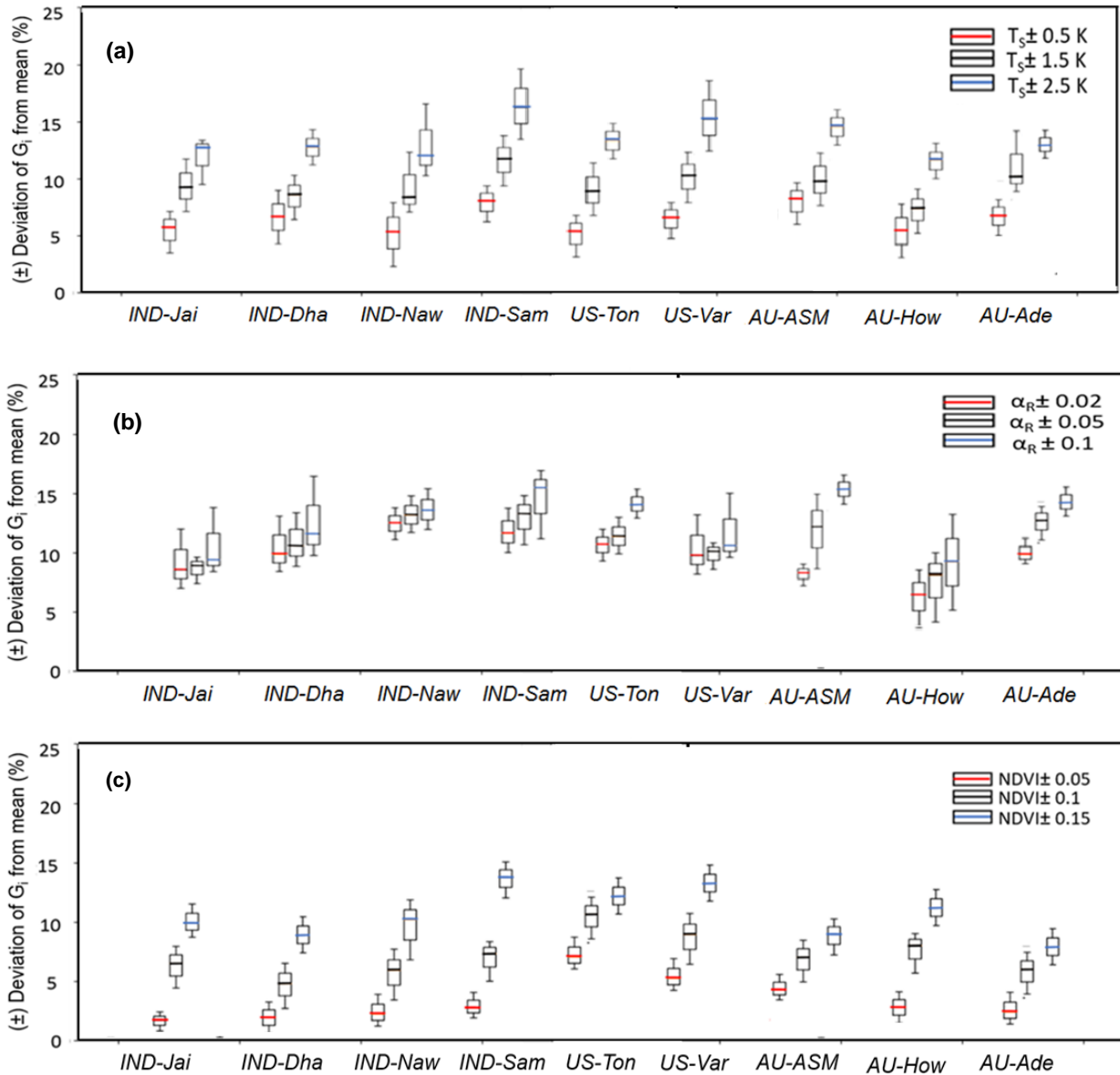


Figure 6: Sensitivity of STIC-TI G_i due to uncertainties in T_s (a), α_R (b), and NDVI (c) for eight flux tower sites in India and Australia. The uncertainties were introduced by taking the mean values of these variables during three different periods (summer, rainy and winter) of a year. Mean uncertainties of the three periods are presented in the figure.

625 **Table 3:** Sensitivity (in percent) of LE_i and H_i due to T_s , NDVI, and α_R uncertainties

Study Sites	Sensitivity of LE_i and H_i to T_s , NDVI and α_R (% range)					
	T_s uncertainty ($\pm 0.5 - 2.5 K$)		α_R uncertainty ($\pm 5 - 10\%$)		NDVI uncertainty ($\pm 0.05 - 0.15$)	
	LE_i	H_i	LE_i	H_i	LE_i	H_i
IND-Jai	2-28	1-6	3-14	2-13	2-8	2-6
IND-Dha	3-26	2-8	2-12	3-12	3-10	3-9
IND-Naw	1-20	2-28	2-10	3-10	2-7	2-6
IND-Sam	1-16	5-32	4-13	6-11	2-5	2-7
US-Ton	4-29	4-12	3-12	4-12	3-8	5-7
US-Var	3-26	6-14	4-11	2-10	4-10	2-8
AU-ASM	5-21	2-10	3-12	2-13	2-10	2-11
AU-How	8-13	2-15	2-11	4-16	3-12	3-13
AU-Ade	2-17	8-17	3-12	2-10	3-10	3-9

626

627 **4.3 Comparative evaluation of STIC-TI and contemporary G_i models**

628 The performances of STIC-TI and existing G_i models were evaluated and compared with respect
629 to *in-situ* G_i measurements. The existing models reported by Moran et al. (1989), Bastiaanssen et
630 al. (1998), Su (2002), and Boegh et al. (2004) have been considered for comparing with TI-based
631 model. These four existing models are referred here as MOR89, BAS98, SU02 and BO04,
632 respectively. While the models MOR89, SU02 and BO04 are based on linear regression between
633 G versus NDVI, BAS98 is based on multivariate regression of G with NDVI, LST and α_R . The
634 performance of the STIC-TI was substantially better as compared to MOR89, SU02 and BO04
635 with respect to MAPD (19%), RMSE (22 Wm^{-2}) and coefficient of determination ($R^2 = 0.8$) when
636 compared with *in-situ* measurements over one Indian, three Australian and two US flux tower sites
637 (Table 4) and also comparable with BAS98 G_i model. The validation plot of retrieved noontime
638 G_i from STIC-TI is shown in Fig. 7.

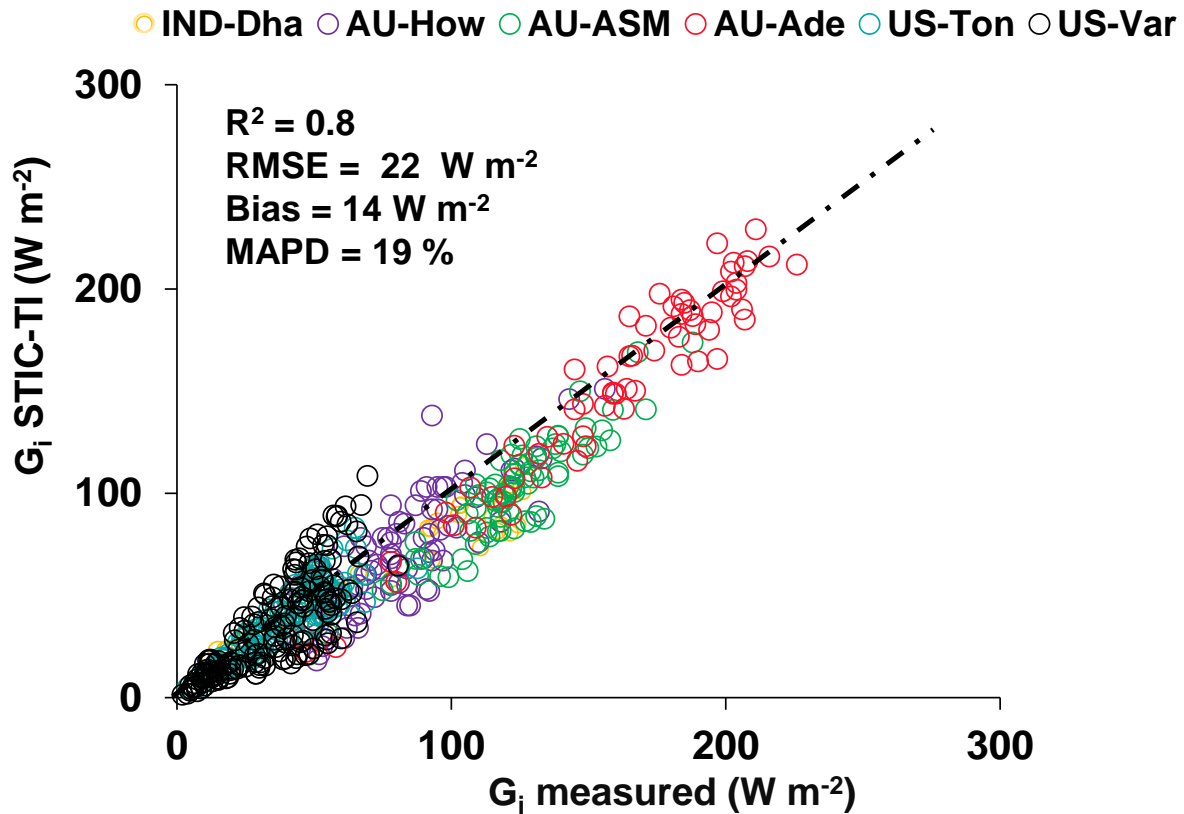


Figure 7: Validation of STIC-TI derived G_i estimates with respect to *in-situ* measurements in different ecosystems. The regression between the two sources of G_i is G_i (STIC-TI) = 0.90 G_i (tower) - 0.10.

639 **Table 4:** A comparison of error statistics of G_i estimates from STIC-TI and existing G_i models
640 over different ecosystems

G models	R²	RMSE (W m⁻²)	MAPD (%)	KGE
STIC-TI	0.80	22	19	0.74
MOR89	0.70	31	29	0.46
BAS98	0.80	20	18	0.61
SU02	0.80	30	26	0.54
BO04	0.70	35	29	0.48

641 The RMSE varied from 9 to 20 W m⁻² with MAPD ranging from 12 to 21% across individual flux
642 tower sites. High magnitude of G_i was predicted in the arid and semi-arid systems (120 – 240 W
643 m⁻²) as compared to the humid systems (20 – 90 W m⁻²), which was in close correspondence with
644 the observations. The model also captured the range of G_i that are generally found in different
645 biomes (20 – 140 W m⁻² for grasslands, 20 – 90 W m⁻² for cropland) (Purdy et al., 2016). Due to

646 the paucity of G_i measurements, direct validation of G_i was only possible for 32 days (concurrent
 647 to MODIS overpass) at the IND-Dha site. Overall, STIC-TI tends to provide reasonable G
 648 estimates for the terrestrial ecosystems having soil temperature amplitude above 5°C .

649 4.4 Evaluation of STIC-TI LE_i , H_i , and EF

650 The modelled versus measured LE_i and H_i showed good agreement in all the nine ecosystems with
 651 RMSE in LE_i and H_i estimates using MYD11 LST product to the order of 29 – 62 W m^{-2} and 26 –
 652 61 W m^{-2} , MAPD of 9 – 31% and 20 – 36%, BIAS of -29 to 38 W m^{-2} and -44 to 32 W m^{-2} (Fig.
 653 8a, b; Table 5) and high R^2 of 0.8.

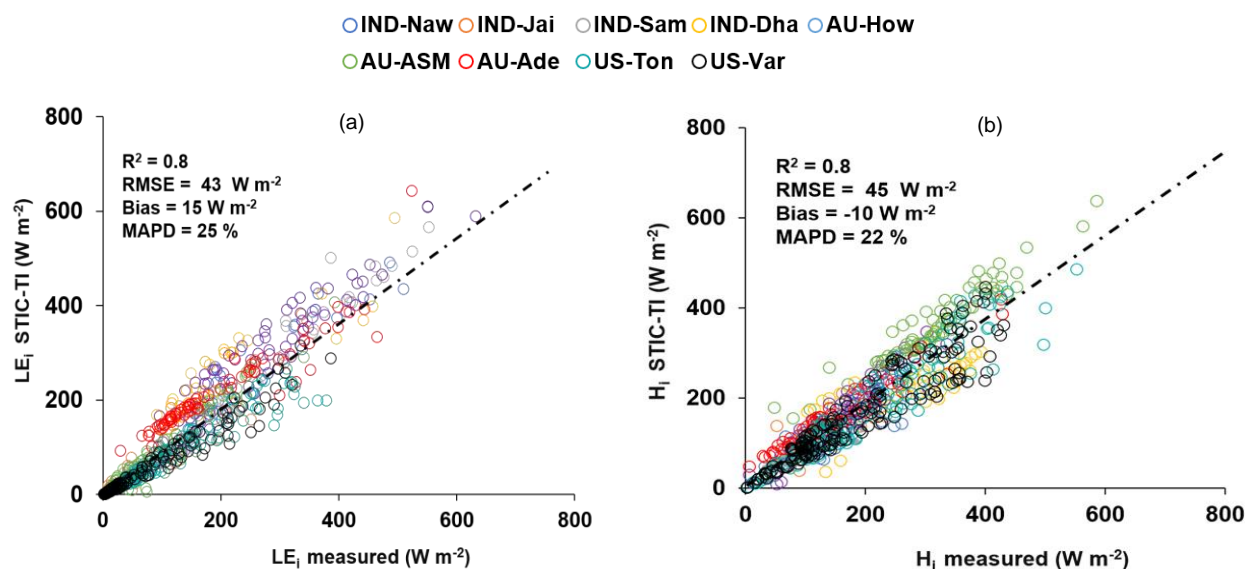


Figure 8: (a) Validation of STIC-TI LE_i estimates with respect to *in-situ* measurements in different ecosystems.; (b) Validation of STIC-TI H_i estimates with respect to *in-situ* measurements in different ecosystems.

654
 655 **Table 5:** Error statistics of STIC-TI LE_i and H_i estimates with respect to EC measurements in
 656 different ecosystems of India, US, and Australia using MYD11A2 LST product for all nine sites
 657 and using MYD21A2 LST product for three semi-arid and arid sites. The statistics obtained by
 658 using MYD21A2LST are shown in the parentheses.

Sites	STIC-TI (LE_i and H_i)									
	R2		BIAS (W m^{-2})		RMSE (W m^{-2})		MAPD (%)		KGE	
	LE_i	H_i	LE_i	H_i	LE_i	H_i	LE_i	H_i	LE_i	H_i
IND-Jai	0.90 (0.91)	0.90 (0.92)	-21 (-16)	12 (9)	57 (45)	27 (21)	31 (24)	22 (19)	0.80 (0.82)	0.76 (0.79)

<u>IND-Naw</u>	<u>0.90</u> (0.92)	<u>0.80</u> (0.85)	<u>19</u> (12)	<u>-26</u> (-16)	<u>44</u> (37)	<u>51</u> (46)	<u>17</u> (16)	<u>28</u> (25)	<u>0.92</u> (0.92)	<u>0.71</u> (0.73)
<u>IND-Dha</u>	<u>0.90</u>	<u>0.90</u>	<u>38</u>	<u>-44</u>	<u>43</u>	<u>35</u>	<u>27</u>	<u>25</u>	<u>0.71</u>	<u>0.64</u>
<u>IND-Sam</u>	<u>0.90</u>	<u>0.80</u>	<u>12</u>	<u>-10</u>	<u>32</u>	<u>61</u>	<u>9</u>	<u>27</u>	<u>0.95</u>	<u>0.70</u>
<u>US-Ton</u>	<u>0.90</u> (0.91)	<u>0.90</u> (0.92)	<u>-29</u> (-18)	<u>-32</u> (-21)	<u>53</u> (45)	<u>34</u> (27)	<u>25</u> (22)	<u>17</u> (15)	<u>0.85</u> (0.87)	<u>0.91</u> (0.93)
<u>US-Var</u>	<u>0.90</u>	<u>0.80</u>	<u>-19</u>	<u>-28</u>	<u>49</u>	<u>39</u>	<u>27</u>	<u>20</u>	<u>0.82</u>	<u>0.89</u>
<u>AU-ASM</u>	<u>0.90</u> (0.93)	<u>0.90</u> (0.91)	<u>-3</u> (6)	<u>22</u> (16)	<u>46</u> (37)	<u>26</u> (18)	<u>29</u> (24)	<u>20</u> (17)	<u>0.94</u> (0.95)	<u>0.83</u> (0.85)
<u>AU-How</u>	<u>0.90</u>	<u>0.90</u>	<u>16</u>	<u>-25</u>	<u>42</u>	<u>27</u>	<u>17</u>	<u>21</u>	<u>0.89</u>	<u>0.85</u>
<u>AU-Ade</u>	<u>0.90</u>	<u>0.90</u>	<u>21</u>	<u>15</u>	<u>29</u>	<u>53</u>	<u>28</u>	<u>36</u>	<u>0.77</u>	<u>0.80</u>

659

660

661

Table 5: Error statistics of STIC-TI LE_i and H_i estimates with respect to EC measurements in different ecosystems of India, US, and Australia.

Sites	STIC-TI (LE_i and H_i)									
	R^2		BIAS ($W\cdot m^{-2}$)		RMSE ($W\cdot m^{-2}$)		MAPD (%)		KGE	
	LE_i	H_i	LE_i	H_i	LE_i	H_i	LE_i	H_i	LE_i	H_i
IND-Jai	0.87	0.85	-21	12	57	27	31	22	0.80	0.76
—IND-Naw	0.89	0.85	19	-26	44	51	17	28	0.92	0.71
IND-Dha	0.92	0.91	38	-44	43	35	27	25	0.71	0.64
IND-Sam	0.85	0.81	12	-10	32	61	9	27	0.95	0.70
US-Ton	0.86	0.88	-29	-32	53	34	25	17	0.85	0.91
US-Var	0.84	0.79	-19	-28	49	39	27	20	0.82	0.89
AU-ASM	0.91	0.89	-3	22	46	26	29	20	0.94	0.83

AU-How	0.88	0.86	16	-25	42	27	17	21	0.89	0.85
AU-Ade	0.86	0.85	21	15	29	53	28	36	0.77	0.80

662

663 Arid ecosystems in India (IND-Jai), US (Ton and Var) and semi-arid ecosystem in Australia (AU-
664 ASM) revealed relatively high MAPD (31%, 25%, 27%, and 28%) (Table 5). In general, STIC-TI
665 was able to produce the dominant convective heat fluxes with respect to the EC measurements as
666 evident through low RMSE for H_i and high RMSE for LE_i in the IND-Jai, US-Ton, US-Var, and
667 AU-Ade where LE_i is inherently low except few rainy days. A uniform distribution of data points
668 around 1:1 validation line (Fig. 8a) indicated overall low BIAS in LE_i estimates. However,
669 modeled H_i was consistently lower than the observations (negative BIAS) in the tropical savanna
670 (IND-Dha and AU-How) and semi-arid (IND-Naw) ecosystems [(-44) – (-25) $W m^{-2}$ and -26 W
671 m^{-2}] while a consistent positive BIAS was observed in the AU-ASM (semi-arid) and AU-Ade
672 (savanna), US-Var (arid) (Fig. 8b; Table 5). This consequently led to overall low negative BIAS
673 ($-10 W m^{-2}$), relatively low R^2 in H_i ($R^2 = 0.8$) as compared to the errors in LE_i (BIAS = 15 $W m^{-2}$,
674 $R^2 = 0.9$). The regression between the modeled and tower measurements of LE_i is $LE_i(STIC-TI)$
675 $= 0.98LE_i(tower) - 0.266$. The regression between the modeled and tower measurements of H_i is
676 $H_i(STIC-TI) = 0.93H_i(tower) + 4.90$. The KGE statistics varied in the range of 0.71 – 0.95 for LE_i
677 and in the range of 0.64 – 0.91 for H_i , respectively across all nine flux tower sites, thus revealed
678 reasonably high efficiency of the model to capture the magnitude and variability of SEB fluxes.

679 The effects of day-night view angle of MODIS Aqua on STIC-TI were further investigated, where
680 the percent deviations in LE_i , H_i and G_i with respect to measurements were analysed in response
681 to the day and night view angle distributed over 12 angular bins within $\pm 50^\circ$ at 10° interval.
682 Number of occurrences of deviations in each bin of day view angle are plotted in Figure F (Refer
683 Appendix F), which showed similar near normal distribution of the three fluxes with G_i deviation
684 having less peak occurrence as compared to the other two. This is due to a smaller number of
685 available datasets used in case of G_i . It has been found that 90% of deviations occur within -40° to
686 30° day view angle thus showing some impact of day view angle on the modeled fluxes. The night
687 view angle variation apparently had no impact on the modelled fluxes.

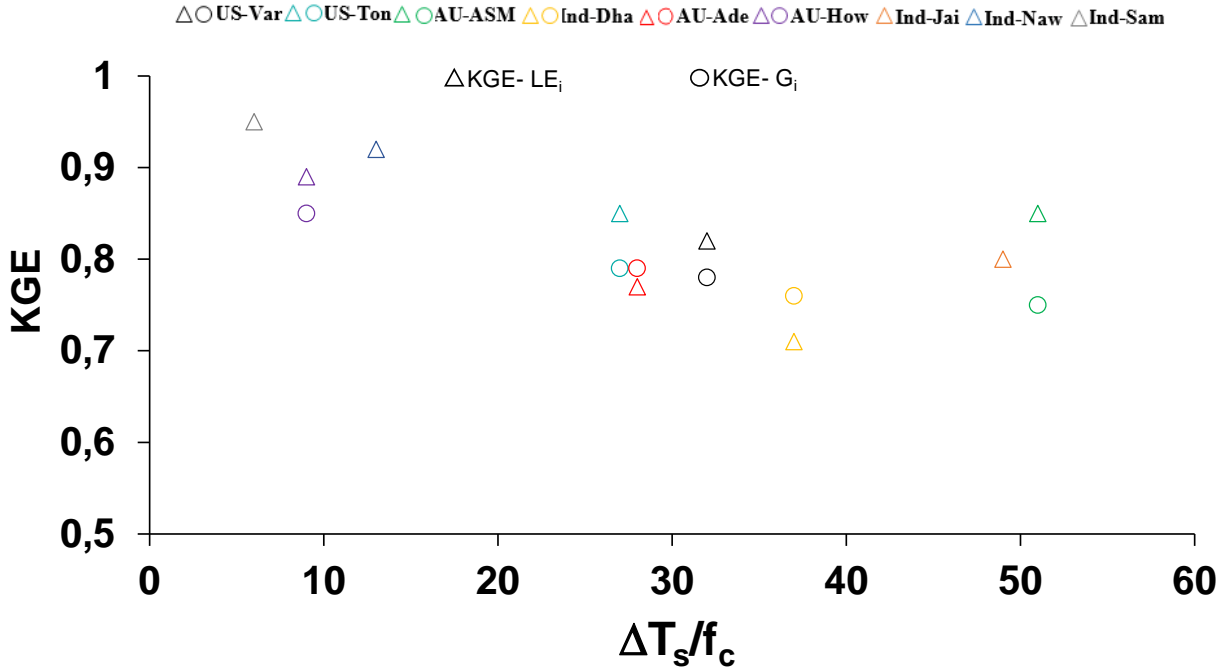


Figure 9: Relationship between KGE of STIC-TI (G_i and LE_i) with $\Delta T_s/f_c$ in different terrestrial ecosystems.

688 Further investigation was made on whether KGE for STIC-TI G_i and LE_i follow any systematic
689 pattern and the ratio ΔT_s and f_c was used as proxy for surface heterogeneity and dryness. The plot
690 of KGE of G_i and LE_i with this ratio is shown in Fig. 9. KGE- G_i was found to show a systematic
691 decrease with increase in ΔT_s - f_c ratio up to 40, after which it remained unchanged with increase
692 in the ratio. Although KGE of LE_i also decreased (20% reduction) with increase in ΔT_s - f_c ratio,
693 KGE- LE_i was found to increase beyond ΔT_s - f_c 40. This revealed that the model efficiency
694 remained high (>0.8) within certain dryness limits (ΔT_s - f_c ratio <20 and >50) and the efficiency
695 reduced moderately (within $0.7 - 0.8$) for intermediate dryness. Interestingly, the use of
696 MYD21A2 LST in STIC-TI showed improvements (see the parentheses in different columns in
697 Table 5) in LE_i and H_i error statistics as compared to using MYD11A2 LST in terms of higher R^2
698 and KGE, and lower RMSE in LE_i (3-8% less) and H_i (2-3% less) for semi-arid and arid sites such
699 as IND-Jai, IND-Naw and US-Ton.

700 An independent evaluation of multi-temporal heat fluxes over two US flux sites for the years 2016-
701 2018 is shown in Fig. 10 and Fig. 11. STIC-TI G_i estimates with MYD11A2 LST product showed
702 close match with *in-situ* measurements with respect to intra and inter-annual variability in G_i

703 followed by LE_i and H_i . This further demonstrates the merit of the coupled model for reproducing
 704 ecosystem-scale G_i estimates especially for shorter and open canopies.

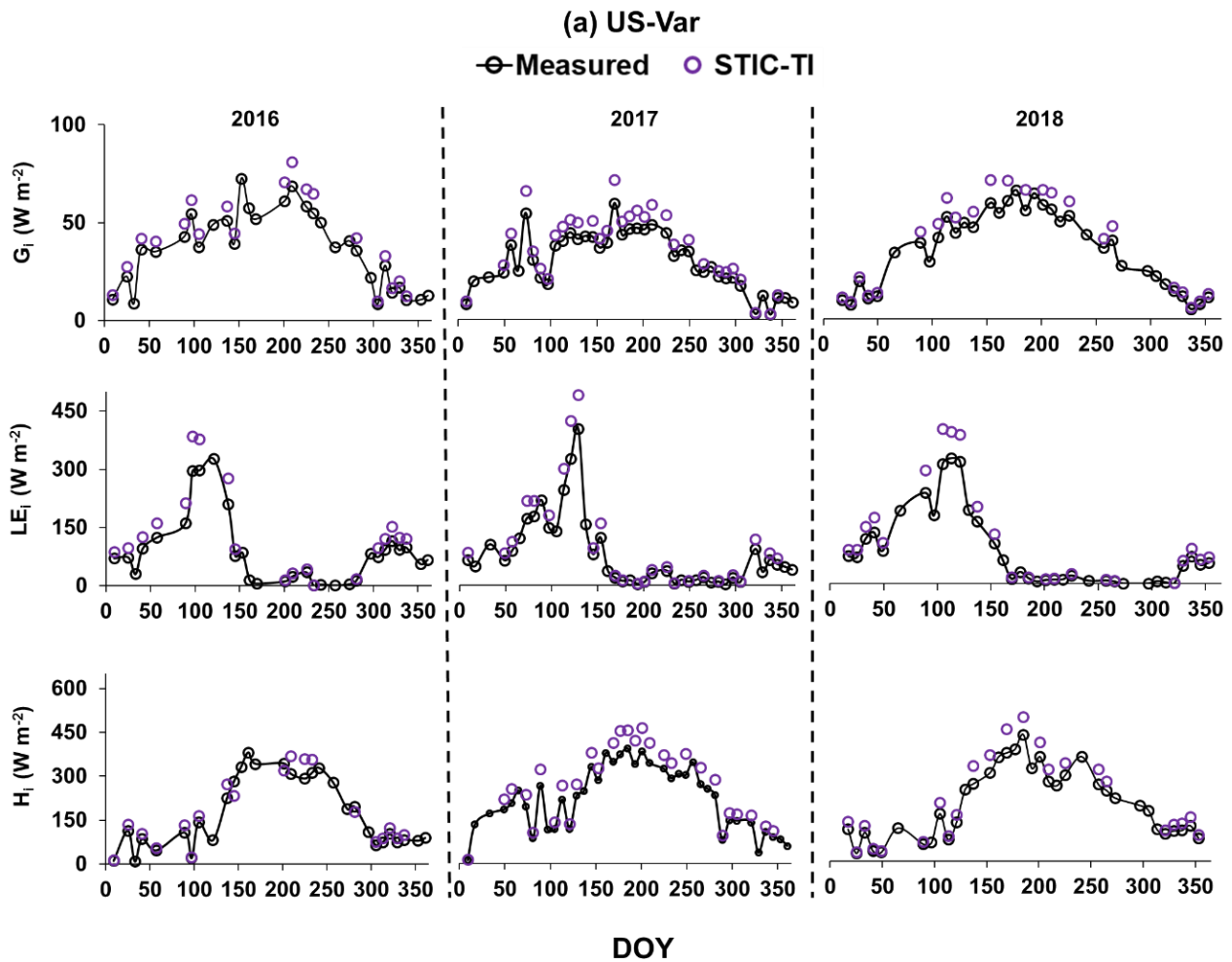


Figure 10: Illustrative examples of temporal evolution of [STIC-TI derived fluxes using MYD11A2 LST product](#) versus observed SEB fluxes for three consecutive years from 2016 to 2018 in a grassland ecosystem in United States (e.g., US-Var).

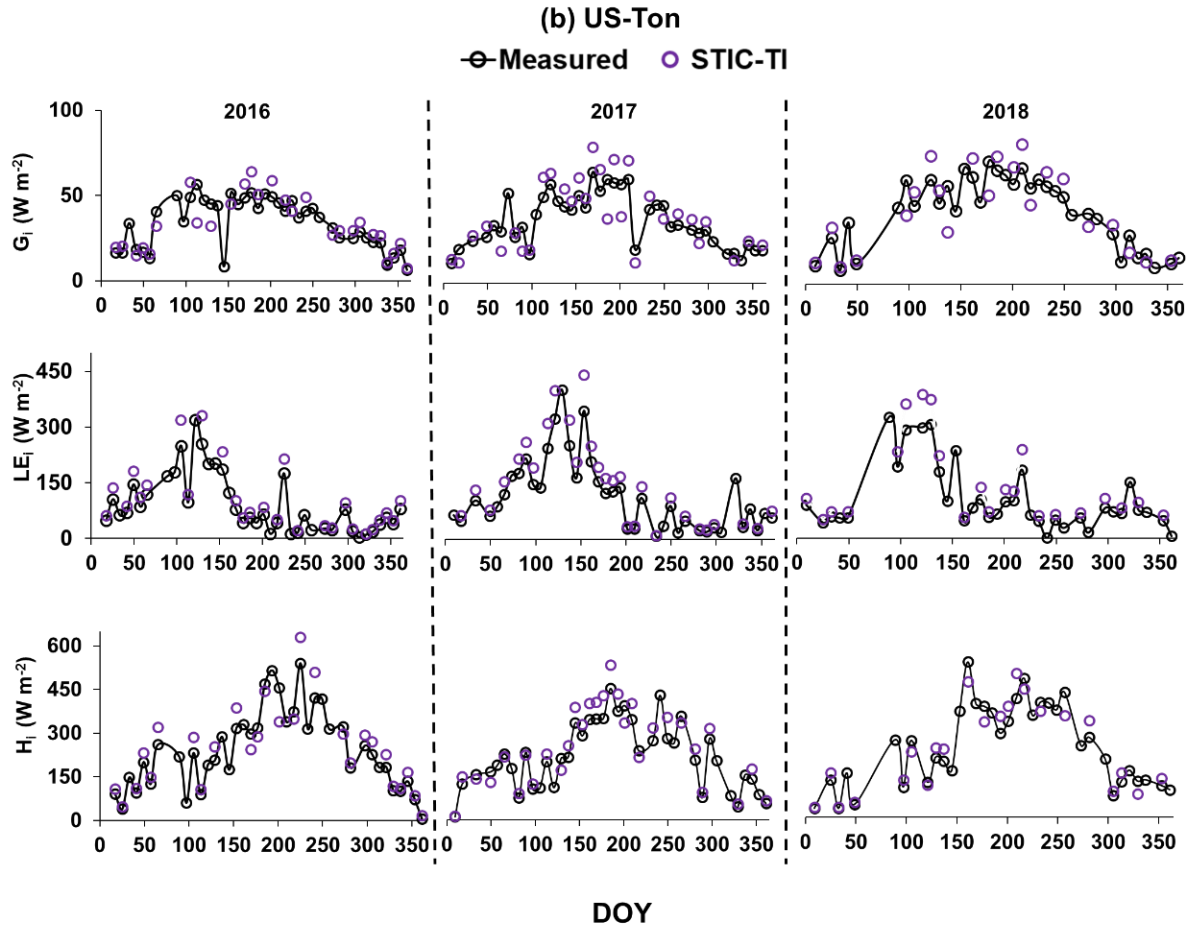


Figure 11: Illustrative examples of temporal evolution of STIC-TI derived fluxes using MYD11A2 LST product versus observed SEB fluxes for three consecutive years from 2016 to 2018 in a woody savanna ecosystem in the United States (e.g., US-Ton).

705 Temporal behavior of STIC-TI and observed evaporative fraction (EF) (ratio of LE and $R_N - G$)
 706 (Fig. 12) along with observed monthly rainfall (P) distinctly captured the substantial temporal
 707 variability in EF during the dry-to-wet transition in the Indian study sites, which also corresponded
 708 to low (high) θ and P. In IND-Naw and IND-Sam, a marked rise (>0.4) in STIC-TI EF was noted
 709 during day-of-the-year (DOY) 25 to 75 where wheat is grown under assured irrigation. The impact
 710 of irrigation is thus captured by the substantial increase in EF in the absence of P. In contrast, the
 711 rainfed grassland system (IND-Jai) showed peak EF (~ 0.8), which corresponded to south-west
 712 monsoon rainfall during June to September and a progressive decline in EF during the dry down
 713 period in October to April corresponding to post south-west monsoon phase. Some intermittent
 714 spikes in EF were also noted during dry-down phase in both STIC-TI and observations. The
 715 intermittent EF spikes during the soil moisture dry down phase could be due to enhanced LE

716 through moisture advection from the surrounding vegetation causing an enhancement of
 717 evaporation than expected. This is known as the ‘clothesline effect’ which frequently occurs in
 718 semi-arid and arid ecosystems.~~This could be due to extra latent heat energy transported through~~
 719 ~~micro-advection from surrounding irrigated agricultural land through the ‘clothesline effect’ which~~
 720 ~~frequently occurs in semi-arid and arid ecosystems.~~ In addition to IND-Jai, the response of both
 721 modelled and measured EF to wet and dry spells was also noted during south-west monsoon period
 722 at all other flux tower sites of India.

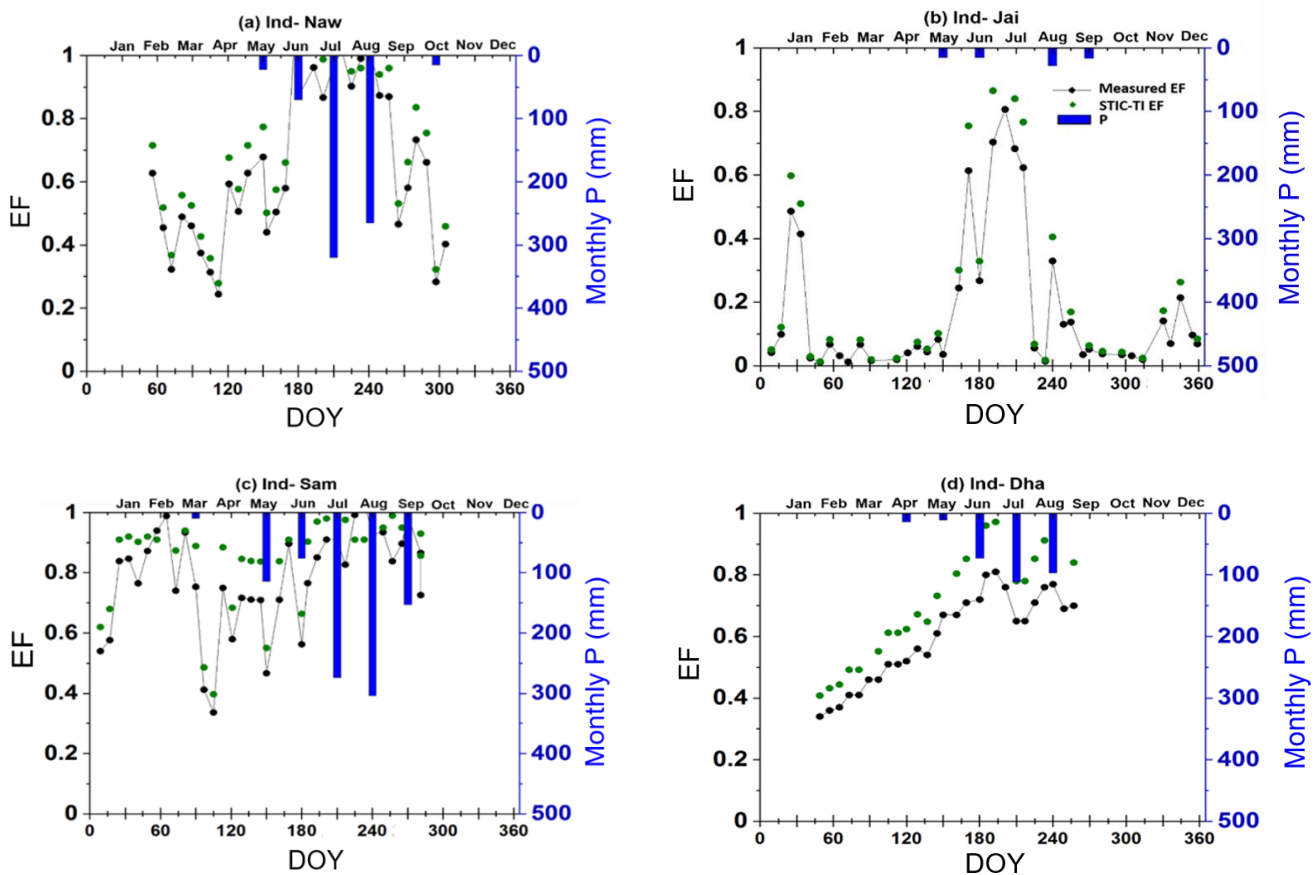


Figure 12: Illustrative examples of temporal variation of STIC-TI derived EF using MYD11A2 LST product with respect to measured EF and P in (a) IND-Naw, (b) IND-Jai, (c) IND-Sam, and (d) IND-Dha

723 The temporal behavior of EF from STIC-TI using MYD11A2 LST product and EC measurements
 724 along with measured θ and P at the OzFlux and AmeriFlux sites also revealed (Fig. 13) close
 725 correspondence of STIC-TI with EC observations. Low EF (0.05 – 0.40) during the dry season
 726 around DOY 100 – 250 and high EF (>0.4) during the wet season (DOY 1 – 120 and 300 to 360)
 727 in AU-ASM, US-Ton and US-Var was observed. The analysis showed that STIC-TI EF can

728 capture the annual variability of observed EF and its responses across different ecosystems during
 729 wet and dry seasons. The plots of STIC-TI EF versus measured θ (in the inset of Fig. 11b) revealed
 730 triangular scatter close to right-angled triangle with positive slope of hypotenuse in three
 731 ecosystems AU-ASM, US-Var and US-Ton. This showed that in the water-controlled ecosystems,
 732 where distinct wet-dry seasons exist, the positive EF- θ relationship is an outcome of the soil
 733 moisture controls on transpiration during the dry season.

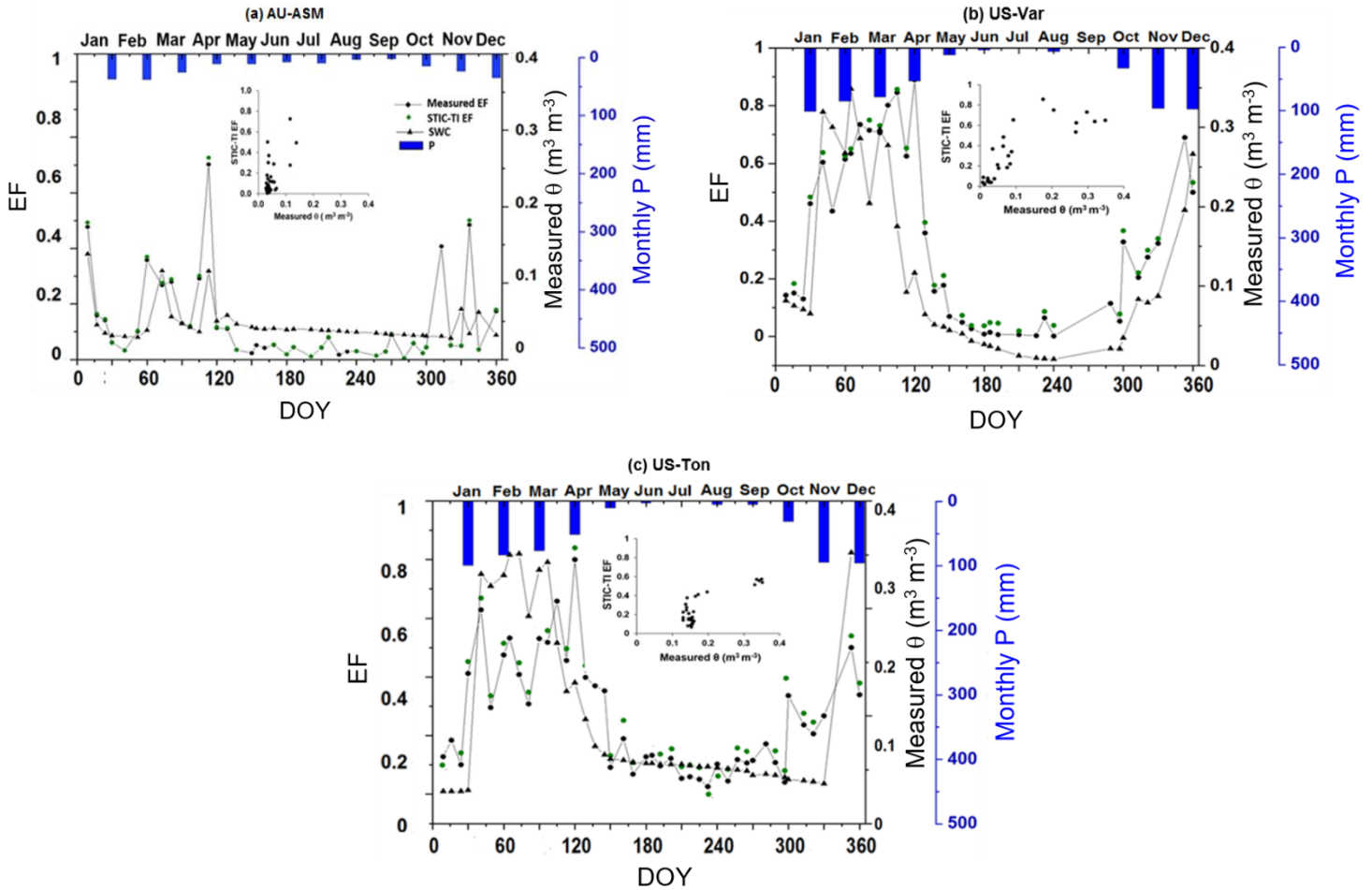


Figure 13: Comparison of temporal variation of STIC-TI derived EF [MYD11A2 LST](#) with respect to measured EF, θ and P in (a) AU-ASM, (b) US-Var, (c) US-Ton. The scatterplots in the inset shows the relationship between STIC-TI EF with respect to measured θ .

734 **5 Discussion**

735 **5.1 Interaction of flux and internal SEB metrics**

736 From the section 4.1 we found relatively reduced sensitivity of G_i to T_s uncertainties. In any given
737 condition, if an over(under) estimation of M due to noontime T_s uncertainties (through eq. 13)
738 leads to an over(under) estimation of Γ , the effects of such over(under) estimation of Γ (due to
739 noontime T_s uncertainties) tend to be compensated by the under(over) estimation of amplitude A
740 (in eq. 5) (Fig. 12d), ultimately leading to a reduction of the sensitivity of G_i to T_s . While the
741 scatter between G versus A for a wide range of Γ (Fig. 14a) revealed large scatter with increasing
742 amplitude under the dry conditions (low Γ), the scatter between Γ versus T_s for different M (Fig.
743 14b) revealed exponential reduction of Γ with increasing T_s and dryness, and almost no significant
744 change in Γ with increasing T_s at a constantly high dryness ($M < 0.25$). Thus, the confounding
745 effects of Γ , A , and M through eq. 3, 5, 12 and 13 led to a reduction of sensitivity of G to T_s , as
746 exemplified in Fig. 14. While the scatter between Γ - M and Γ - T_s (Fig. 12a, b) revealed the
747 sensitivity of G_i to T_s in arid (IND-Jai) and tropical savannah (IND-Dha); which were due to the
748 strong relationship between Γ and daytime T_s (Fig. 12b); the scatter between G_i , Γ , and A (Fig.
749 12c, d) revealed that the sensitivity of G_i to T_s in semi-arid (IND-Naw) and sub-humid (IND-Sam)
750 ecosystems were due to the strong association between G_i and A .

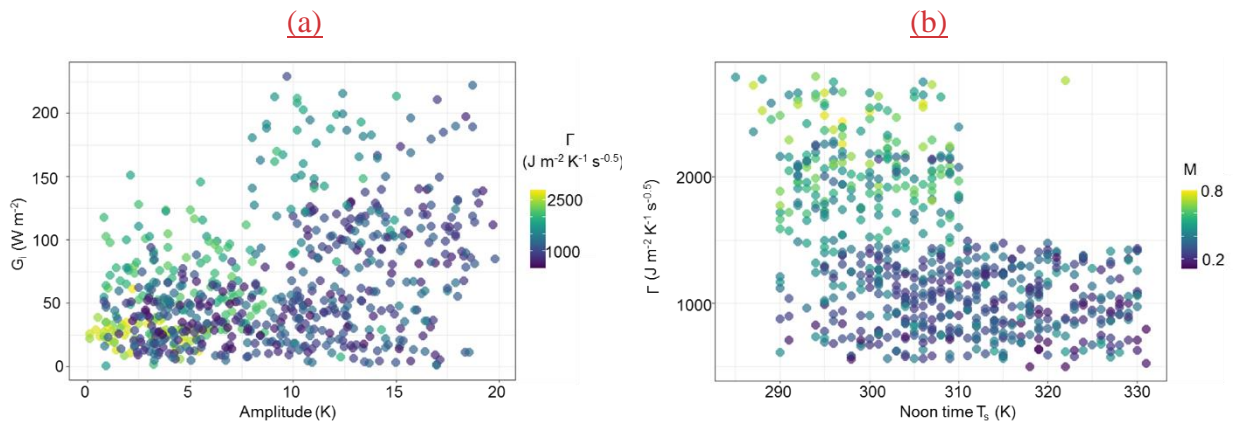


Figure 14: Response plots among parameters of TI-based G_i model, such as (a) G_i versus Amplitude (A) for varying Γ , and (b) Noon-time T_s versus Γ with varying M .

751
752
753

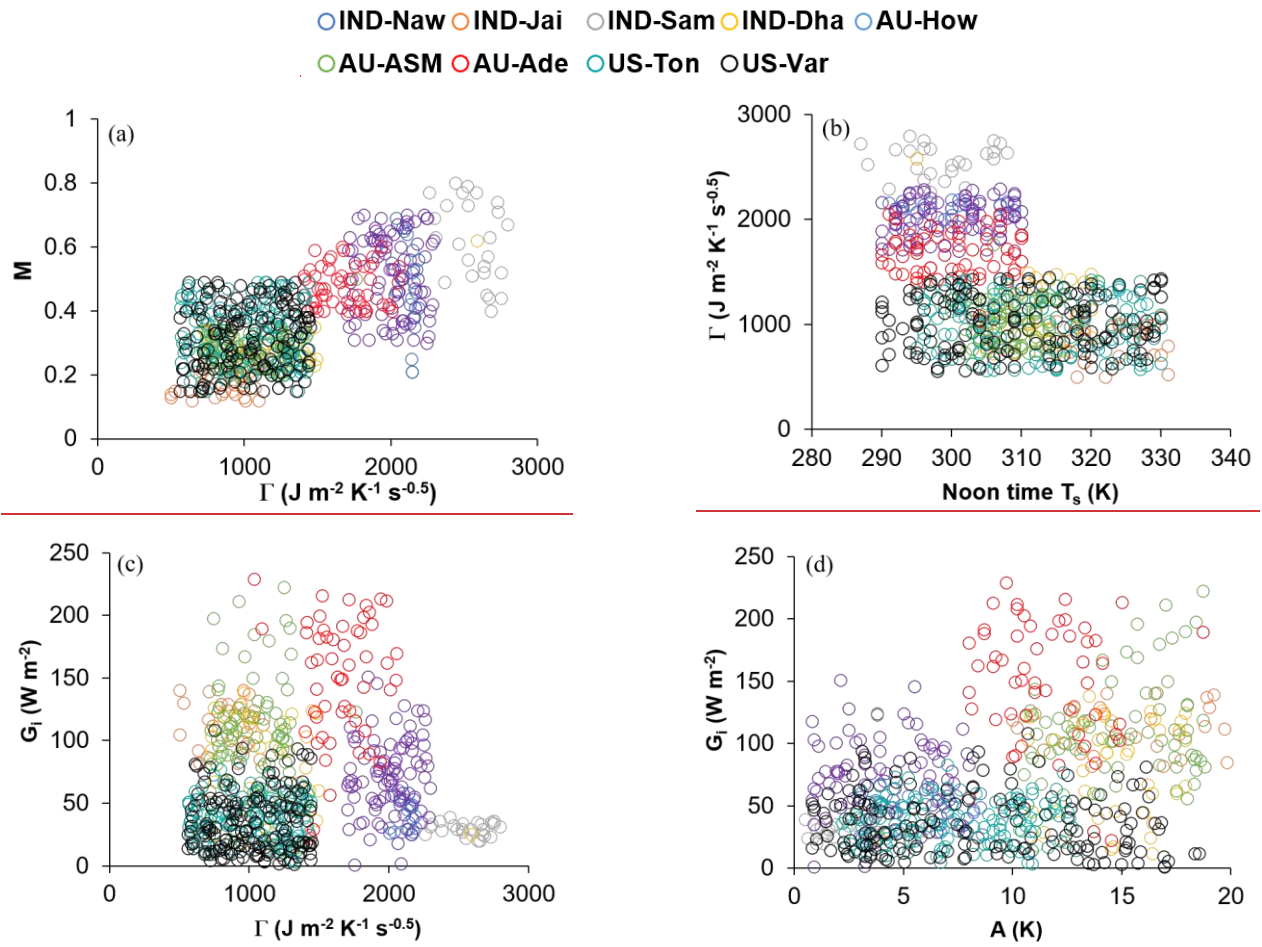


Figure 12: Response plots among parameters of TI-based G_i model, such as (a) Γ vs. M , (b) Γ vs. noon-time T_s , (c) G_i vs. Γ , and (d) G_i vs. A over different ecosystems.

755 Concerning LE_i and H_i , dual uncertainties could be propagated in both the fluxes through
 756 daytime T_s (through M and G_i), leading to high sensitivity of these two SEB fluxes due to T_s
 757 perturbations. The relatively high sensitivity of LE_i to T_s (as compared to H_i) in the non-
 758 irrigated ecosystems could be due to partial compensation of g_A/g_s in both numerator and
 759 denominator of the PMEB equation for H (eq. C7 of Appendix C). A recent study (Fig.10 in
 760 Mallick et al., 2018a) showed high sensitivity of g_s due to T_s (1% change in T_s led to 5.2–7.5%
 761 change in g_s) as compared to g_A sensitivity to T_s (1% change in T_s led to 1.6–2% change in g_A),
 762 suggesting that errors in g_s due to T_s uncertainty tend to be larger than errors in g_A . Partial
 763 cancellation of the conductance errors in the numerator of eq. (C7 of Appendix C) might have
 764 resulted in compensation of H_i errors in the water-limited ecosystems. In this environment, the

765 variability of LE_i is mainly dominated by g_A/g_S , which makes LE_i highly sensitive due to T_S
766 uncertainties. Combined uncertainty due to g_A/g_S in the denominator and g_A in the numerator
767 of eq. (C6 of Appendix C) resulted into greater sensitivity in LE_i to T_S in the arid and tropical
768 savannah ecosystems (Mallick et al., 2015, 2018a; Winter & Eltahir, 2010). The very low
769 sensitivity of LE_i and H_i due to uncertainties in NDVI is because NDVI was not used in the
770 conductance parameterizations and effects due to NDVI in STIC-TI was only propagated
771 through G_i . The sensitivity of LE_i and H_i to albedo was mainly due to the dependence of net
772 radiation (R_{Ni}) on albedo, and any resultant uncertainty in R_{Ni} (due to albedo) tends to be
773 reflected in the sensitivity of LE_i and H_i to albedo.

774 5.2 Possible sources of errors in SEB flux evaluation

775 In STIC-TI, underestimation and overestimation errors in G_i in different ecosystems (Fig. 7) could
776 originate due to the errors in ~~MYD11A2MOD11A1~~ LST product. A host of studies previously
777 reported that the standard deviations of errors in retrieved emissivity in bands 31 and 32 are 0.009,
778 and the maximum error in retrieved T_S of MOD11A1 LST falls within 2-3 K, which is mainly due
779 to the errors in surface emissivity correction (Duan et al., 2017; Wan, 2014; Lei et al., 2018). A
780 host of studies previously reported T_S error of MOD11A1 LST product in the range of 2-3 K with
781 a standard deviation of 0.009, which is mainly due to errors in surface emissivity correction (Duan
782 et al., 2017; Wan, 2014; Lei et al., 2018). In the present analysis, we found an overestimation error
783 of MODIS T_S in the range of 0.5 – 1.5 K when compared with *in-situ* infrared temperature
784 measurements at the tropical savanna site. As mentioned in section 3.1, a positive (negative) bias
785 in T_S would tend to an overestimation (underestimation) of amplitude (A) in eq. (5);
786 underestimation (overestimation) of M in eq. (13), and consequent underestimation
787 (overestimation) of Γ (eq. 12) and G_i , respectively. Furthermore, the standard deviation of NDVI
788 surrounding the tower sites varied from 0.01 – 0.05 when compared to the ground measurements,
789 which could be another source of error in the STIC-TI model. In addition, NDVI saturates at LAI
790 > 3 . However, STIC-TI provides direct estimates of ecosystem G and is independent of R_N .
791 Despite the comparable accuracy of current G estimates with the G model of Bastiaanssen et al
792 (1998), the foundation of STIC-TI lies in the use of soil moisture characteristics with varying soil
793 textural types which are known to influence the soil heat conductance and thereby G. Thus, the
794 control of soil moisture on evaporation is explicitly included in STIC-TI as opposed to the semi-

795 empirical G function of Bastiaanssen et al (1998). The higher accuracies of TI-based thermal
796 diffusion model as compared to R_N dependent empirical G models were also reported by Purdy et
797 al. (2016) at daily or longer time scales in cropland, grassland. All these G model estimates many
798 a times differ from in situ measurements because of the no accounting of leaf litter presence or
799 layer on soil floor in the remote sensing-based G-model.

800 The overestimation (underestimation) of LE_i (H_i) is also due to the effects of spatial resolution of
801 different input variables on these two SEB fluxes and conducted statistical evaluation with respect
802 to the measured SEB fluxes. Eswar et al. (2017) demonstrated the need for spatial disaggregation
803 models for monitoring LE_i at field scale using contextual models by disaggregation of evaporative
804 fraction (Λ) and downwelling shortwave radiation ratio (R_G). Using different disaggregation
805 models, they estimated LE_i at 250m spatial resolution and reported RMSE of $30 - 32 \text{ W m}^{-2}$ as
806 compared to LE_i obtained at 1000m spatial resolution with RMSE of $40 - 70 \text{ W m}^{-2}$ over different
807 sites in India. Anderson et al. (2007) reviewed different validation experiments conducted in
808 diverse agricultural landscapes (Anderson et al., 2004, 2005; Norman et al., 2003) and reported
809 RMSE in LE_i in the range of $35 - 40 \text{ W m}^{-2}$ (15%) at $30 - 120 \text{ m}$ disaggregated spatial resolution.
810 Current analysis also brought out the need for noon-night thermal imaging with spatial resolution
811 finer than 1000m to adequately capture the magnitude and variability of LE_i in the terrestrial
812 ecosystems especially agroecosystems where average field sizes are less ($< 0.5 \text{ ha}$) and fragmented
813 such as in India and other sub-continent.

814 As seen in Fig. 8a and Table 5, there is a gross overestimation of LE_i with respect to the tower
815 observations when MYD11A2 LST was used. The consistent positive BIAS in STIC-TI LE_i in
816 five out of nine sites is presumably due to the overestimation of R_{Ni} (Figure B1 of Appendix B)
817 and underestimation of G_i . Figure 7 shows overestimation of G_i for three OzFlux sites and US sites
818 and underestimation of G_i for Indian site with G_i (STIC-TI) = $0.90 G_i(\text{tower}) - 0.10$ and
819 overestimation of R_{Ni} at the ecosystem-scale, with R_{Ni} (STIC-TI) = $0.78R_{Ni}(\text{tower}) + 58.92$
820 (Appendix-B2). This means a systematic overestimation of the net available energy ($R_{Ni} - G_i$) will
821 be obvious in cases where STIC-TI shows underestimation of G_i , which consequently leads to an
822 overestimation of retrieved LE_i . It may be also noted that the use of MYD21A2 LST led to
823 relatively better accuracy in LE_i (3-8%) and H_i (2-3%) as compared to using MYD11A2 LST in
824 semi-arid and arid ecosystems. The higher retrieval accuracy of MYD21A2 LST using TES
825 (Temperature-Emissivity Separation) algorithm over MYD11A2 LST that uses split-window

826 algorithm (Wan et al, 2015) is the main reason for obtaining higher accuracy in LE_i and H_i
827 estimates.

828

829 **5.3 Effects of SEB closure**

830 Given there is a widespread lack of SEB closure ($H + LE \neq R_N - G$) or residual energy balance,
831 knowledge of the impact of different vegetation types and climatic variables on SEB ‘non-closure’
832 is essential. A recent study by Dare-Idowu et al. (2021) covering 8 growing seasons and 3 crops
833 (maize, wheat, and rapeseed) in two sites of south-western France showed that the systematic effect
834 of each site on SEB closure was stronger than the influence of crop type and stage. Same study
835 revealed a greater percentage of SEB closure under unstable atmospheric conditions and in the
836 prevailing wind directions, and sensible heat advection accounted for more than half of the
837 imbalance at both the sites.

838 In our study, Using-using the unclosed SEB observations for Indian sites in absence of *in-situ* G_i
839 observations also added to the consistent positive BIAS in the statistical evaluation of LE_i . A
840 widespread lack of energy balance closure to the order of 10 – 20% worldwide at most of the EC
841 sites is reported in the literature (Stoy et al., 2013; Wilson et al., 2002), which implies a systematic
842 underestimation (overestimation) of LE_i (EC tower) (and/or H_i (EC tower)). Accommodating an
843 average 15% imbalance in LE_i (EC tower) would tend to diminish the positive BIAS in STIC-TI.
844 Therefore, the pooled gain (0.98) and positive BIAS between the STIC-TI and tower LE_i is
845 determined by the overestimation of $(R_{Ni} - G_i)$, combined with the underestimation of measured
846 LE_i from the EC towers. An underestimation of H_i (negative BIAS) is associated with two reasons;
847 (a) ignoring the two-sided aerodynamic conductance of the leaves (Jarvis and McNaughton, 1986;
848 Monteith and Unsworth, 2013; Schymanski et al., 2017), which could lead to substantial
849 underestimation of H_i , and (b) due to the complementary nature of the PMEB equation, if LE_i is
850 overestimated, H_i will be underestimated. In addition, frequent micro-advection fluxes alter
851 measured in situ H and LE fluxes. But these advection conditions are not explicitly accounted in
852 the current STIC-TI model. At the EC tower sites, the fraction of residual energy balance to R_N
853 can be quantified with respect to vegetation/crop growth characteristics or biophysical properties.
854 However, where G observations are lacking such as in many Indian EC tower sites, the TI-based

855 G model can be used to fill up the missing G observations to quantify residual energy balance and
856 to correct the SEB non-closure.

857 **6 Summary and conclusions**

858 This study addressed one of the outstanding challenges in retrieving ground heat flux (G) and
859 evaporation (ET) in open canopy, water-controlled and radiation-controlled ecosystems. It
860 demonstrated coupling of a thermal inertia (TI)-based mechanistic G model with an analytical
861 surface energy balance (SEB) model (Surface Temperature Initiated Closure, STIC) using
862 satellite-based land surface temperature (T_s) and associated biophysical variables and has minimal
863 independence on *in-situ* measurements. The model is called STIC-TI, and this is the first ever
864 implementation of a coupled G-SEB model that does not require any empirical parameterization
865 of aerodynamic (g_A) and canopy-surface (g_s) conductance. The estimation of g_A and g_s in STIC-
866 TI is independent of any parameterization of surface roughness and atmospheric stability and does
867 not involve any look-up table for biome or plant functional attributes. By linking T_s with thermal
868 inertia (Γ) and surface moisture availability (M), STIC-TI derives G through the harmonics
869 equation between G and Γ , and subsequently coupled G with the SEB fluxes. ~~For estimating Γ ,~~
870 ~~this paper also developed scaling functions for ecosystem scale surface soil temperature amplitude~~
871 ~~(A) through bivariate regression between the observed soil temperature versus remote sensing~~
872 ~~derived T_s and surface albedo.~~ Independent validation of STIC-TI using measured flux data from
873 nine terrestrial ecosystems in arid, semi-arid and sub-humid climate in India, USA (representing
874 northern hemisphere) and Australia (representing southern hemisphere) led us to the following
875 conclusions:

876 (i) The retrieved G_i and associated SEB fluxes through STIC-TI were reasonably sensitive to
877 uncertainties in T_s and vegetation index. However, a compensation effect was evident due to
878 the partial cancellation of overestimated TI and underestimated A in the harmonics equation
879 of G. Both, latent and sensible heat fluxes (LE and H), were extremely sensitive to T_s
880 uncertainties. While the maximum sensitivity of LE to T_s was found in the arid and semi-arid
881 ecosystems, the sensitivity of H to T_s was maximum in the sub-humid ecosystems.

882 (ii) G estimates through STIC-TI performed better as compared to most of the contemporary
883 empirical G models, with lower MAPD and higher correlation coefficient with respect to *in-*

884 situ measurements. The most notable advantages of STIC-TI are, (a) it provides direct
885 estimates of G and is not dependent on net radiation estimates, (b) the ecosystem-scale surface
886 soil temperature amplitude used in G model can advance our understanding on associated
887 terrestrial ecosystem processes.

888 ~~(ii) G_i estimates through STIC-TI performed better as compared to most of the contemporary~~
889 ~~empirical G models. It showed lower mean absolute percent deviation (MAPD) of 19% and~~
890 ~~higher correlation coefficient (0.8) with respect to in-situ measurements for different~~
891 ~~ecosystems. Despite the error statistics, G from STIC-TI was comparable to the existing semi-~~
892 ~~empirical G model of Bastiaanssen et al. (1998) (BAS98), this coupled model has certain~~
893 ~~advantages such as, (a) it provides direct estimates of G and is not dependent on net radiation~~
894 ~~estimates, (b) the ecosystem-scale surface soil temperature amplitude used in G model can~~
895 ~~advance our understanding on associated terrestrial ecosystem processes.~~

896 ~~(iii) Overall, the STIC-TI explained significant variability in the measured SEB fluxes with a~~
897 ~~MAPD of 19% for instantaneous G and 22–25% for instantaneous LE and H. The model~~
898 ~~efficiency (KGE) was greater than 0.7 for G and LE in all the nine ecosystems having~~
899 ~~contrasting aridity and canopy cover. Underestimation tendency of G in some ecosystems was~~
900 ~~primarily attributed to the inherent bias in MODIS T_s product, NDVI saturation at higher LAI~~
901 ~~(>3) in conjunction with the spatial scale mismatch between single MODIS pixel and the~~
902 ~~footprint of G measurements. The consequent overestimation (underestimation) of LE (H) in~~
903 ~~some ecosystems was associated with the overestimation of the net available energy, use of~~
904 ~~‘unclosed’ SEB observation in the validation of LE and H, the spatial scale discrepancy~~
905 ~~between MODIS pixel versus eddy covariance measurement footprint, the complementary~~
906 ~~nature of the Penman Monteith Energy Balance equation (for H), and possibly due to ignoring~~
907 ~~the two-sided aerodynamic conductance by the leaves (for H), respectively.~~

908 ~~(iv) While the MODIS Aqua day view angle within -40° to 30° showed moderate impact on the~~
909 ~~deviations in the modeled heat fluxes, the night view angle had no impact on the flux~~
910 ~~deviations.~~

911 The requirement of few input variables in STIC-TI generates promise for surface-atmosphere
912 exchange studies using readily available data from the current generation remote sensing satellites
913 (e.g., MODIS, INSAT) that have noon-night TIR observations. ~~Current findings also provide~~

914 ~~motivation in refining G simulation in the land surface models.~~ STIC-TI can be potentially used
915 for distributed ET mapping using current and future 4th generation Indian Geostationary satellite
916 observations from INSAT as well as future high spatial resolution (~ 60m) TIR observations with
917 3-day revisit from polar orbiting platform (Lagouarde et al., 2018, 2019) through the planned Indo-
918 French space-borne mission, TRISHNA (Thermal infrared Imaging Satellite for High-resolution
919 Natural Resource Assessment). This simple approach will also help in catering the need for a
920 reliable, space-time continuous ET datasets in data-poor regions like Indian sub-tropics, South-
921 East Asia, and other parts of the world from thermal remote sensing observation.

922 **Author contributions**

923 KM and BKB conceptualized the idea; DD conducted STIC-TI model coding, simulations and
924 data analysis in consultation with KM and BKB; DD and BKB wrote the first version of the
925 manuscript with KM writing the introduction, discussions and conclusions; all authors contributed
926 to discussions, editing and corrections; BKB and KM jointly finalized the manuscript.

927 **Acknowledgement**

928 The authors gratefully acknowledge Ministry of Earth Sciences (MoES), Govt. of India and
929 National Environmental Research Council for providing necessary support through Indo-UK
930 INCOMPASS programme (NE/L013819/1, NE/L013843/1, NE/L01386X/1, NE/P003117/1).
931 BKB acknowledges Deputy Director, EPSA, SAC-ISRO and Director, SAC-ISRO for providing
932 necessary support to participate and contribute to Indo-UK INCOMPASS programme. DD
933 acknowledges Prof. P.D. Lele and Head from Department of Physics, Electronics and Space
934 Sciences, Gujarat University Ahmedabad and for providing the necessary support to carry out this
935 work. KM was supported through the International Mobility fellowship of Luxembourg National
936 Research Fund (FNR) (INTER/MOBILITY/2020/14521920/MONASTIC). ~~KM was supported by~~
937 ~~the Luxembourg Institute of Science and Technology (LIST) and through the doctoral training unit~~
938 ~~and through the Mobility OUT fellowship of Luxembourg National Research Fund (FNR)~~
939 ~~(PRIDE15/10623093/HYDROCSI; INTER/MOBILITY/2020/14521920/MONASTIC).~~ KCN is
940 supported by -the Jet Propulsion Laboratory, California Institute of Technology, under contract
941 with the National Aeronautics and Space Administration and Government sponsorship is

942 acknowledged. DDB acknowledges support from NASA Ecostress project and the US Department
943 of Energy, Office of Science which supports the AmeriFlux project

944 **Data and code availability**

945 Harmonized time series datasets over the study grids are available in
946 <https://doi.org/10.5281/zenodo.5806501>. The model code is available to the first author upon
947 reasonable request.

948 **References**

949 Anderson, M., Kustas, W., Alfieri, J., Gao, F., Hain, C., Prueger, J., Evett, S., Colaizzi, P., Howell,
950 T. and Chávez, J.: Mapping daily evapotranspiration at Landsat spatial scales during the
951 BEAREX'08 field campaign, *Adv. Water Resour.*, 50, 162 – 177,
952 <https://doi.org/10.1016/j.advwatres.2012.06.005>, 2012.

953 Anderson, M., Norman, J., Kustas, W., Li, F., Prueger, J. and Mecikalski, J.: Effects of Vegetation
954 Clumping on Two–Source Model Estimates of Surface Energy Fluxes from an Agricultural
955 Landscape during SMACEX, *J. Hydrometeorol.*, 6(6), 892 – 909,
956 <https://doi.org/10.1175/JHM465.1>, 2005.

957 Anderson, M., Norman, J., Mecikalski, J., Otkin, J. and Kustas, W.: A climatological study of
958 evapotranspiration and moisture stress across the continental United States based on thermal
959 remote sensing: 1. Model formulation, *J. Geophys. Res.: Atmos.*, 112(D10),
960 <https://doi.org/10.1029/2006JD007506>, 2007.

961 Anderson, M., Norman, J., Mecikalski, J., Torn, R., Kustas, W. and Basara, J.: A Multiscale
962 Remote Sensing Model for Disaggregating Regional Fluxes to Micrometeorological Scales, *J.*
963 *Hydrometeorol.*, 5(2), 343 – 363, [https://doi.org/10.1175/1525-7541\(2004\)005<0343:AMRSMF>2.0.CO;2](https://doi.org/10.1175/1525-7541(2004)005<0343:AMRSMF>2.0.CO;2), 2004.

965 Bai, Y., Zhang, S., Bhattarai, N., Mallick, K., Liu, Q., Tang, L., Im, J., Guo, L., and Zhang, J: On
966 the use of machine learning based ensemble approaches to improve evapotranspiration
967 estimates from croplands across a wide environmental gradient, *Agric. Forest Meteorol.*, 298
968 - 299, 108308, <https://doi.org/10.1016/j.agrformet.2020.108308>, 2021.

- 969 ~~Zerefos, C. S., & Bais, A. F.: Solar Ultraviolet Radiation: Modelling, Measurements and~~
970 ~~Effects, Springer Berlin Heidelberg, 2013.~~
- 971 Bastiaanssen, W. G. M., Menenti, M., Feddes, R. A. and Holtslag, A. A. M.: A remote sensing
972 surface energy balance algorithm for land (SEBAL). 1. Formulation, J. Hydrol., 198-212,
973 doi:10.1016/S0022-1694(98)00253-4, 1998.
- 974 Bennett, W., Wang, J. and Bras, R.: Estimation of Global Ground Heat Flux, J. Hydrometeorol.,
975 9(4), 744 – 759, <https://doi.org/10.1175/2008JHM940.1>, 2008.
- 976 Beringer, J., Hutley, L. B., McHugh, I., Arndt, S. K., Campbell, D., Cleugh, H. A., Cleverly, J.,
977 Resco de Dios, V., Eamus, D., Evans, B., Ewenz, C., Grace, P., Griebel, A., Haverd, V.,
978 Hinko-Najera, N., Huete, A., Isaac, P., Kanniah, K., Leuning, R., Liddell, M. J., Macfarlane,
979 C., Meyer, W., Moore, C., Pendall, E., Phillips, A., Phillips, R. L., Prober, S. M., Restrepo-
980 Coupe, N., Rutledge, S., Schroder, I., Silberstein, R., Southall, P., Yee, M. S., Tapper, N. J.,
981 van Gorsel, E., Vote, C., Walker, J., and Wardlaw, T.: An introduction to the Australian and
982 New Zealand flux tower network – OzFlux, Biogeosciences, 13, 5895–5916, doi:10.5194/bg-
983 13-5895-2016, 2016.
- 984 ~~Bhandari, A., Kumar, A. & Singh, G.K.: Feature Extraction using Normalized Difference~~
985 ~~Vegetation Index (NDVI): A Case Study of Jabalpur City, Proc Technol., 6, 612–621,~~
986 ~~<https://doi.org/10.1016/j.protey.2012.10.074>, 2012.~~
- 987 Bhat, G., Morrison, R., Taylor, C., Bhattacharya, B., Paleri, S., Desai, D., Evans, J., Pattnaik, S.,
988 Sekhar, M., Nigam, R., Sattar, A., Angadi, S., Kancha, D., Patidar, A., Tripathi, S., Krishnan,
989 K. and Sisodiya, A.: Spatial and temporal variability in energy and water vapor fluxes
990 observed at seven sites on the Indian subcontinent during 2017, Q. J. R. Meteorolog. Soc., 146
991 (731), <https://doi.org/10.1002/qj.3688>, 2853-2866, 2019.
- 992 Bhattarai, N., Mallick, K., Brunzell, N. A., Sun, G., and Jain, M.: Regional evapotranspiration
993 from an image-based implementation of the Surface Temperature Initiated Closure (STIC1.2)
994 model and its validation across an aridity gradient in the conterminous US, Hydrol. Earth Syst.
995 Sci., 22, 2311–2341, <https://doi.org/10.5194/hess-22-2311-2018>, 2018.
- 996 Bhattarai, N., Mallick, K., Stuart, J., Vishwakarma, B., Niraula, R., Sen, S. and Jain, M.: An
997 automated multi-model evapotranspiration mapping framework using remotely sensed and
998 reanalysis data, Remote Sens. Environ., 229, 69 – 92,
999 <https://doi.org/10.1016/j.rse.2019.04.026>, 2019.

- 1000 Boegh, E., Soegaard, H., Christensen, J. H., Hasager, C. B., Jensen, N.O. and Nielsen, N. W.:
1001 Combining weather prediction and remote sensing data for the calculation of
1002 evapotranspiration rates: application to Denmark, *Int. J. Remote Sens.*, 25, 2553 - 2574,
1003 <https://doi.org/10.1080/01431160310001647984>, 2004.
- 1004 Cammalleri, C. and Vogt, J.: On the Role of Land Surface Temperature as Proxy of Soil Moisture
1005 Status for Drought Monitoring in Europe, *Remote Sens.*, 7(12), 16849-16864,
1006 <https://doi.org/10.3390/rs71215857>, 2015.
- 1007 Cano, D., Monget, J., Albuissou, M., Guillard, H., Regas, N. and Wald, L.: A method for the
1008 determination of the global solar radiation from meteorological satellite data. *Solar Energy*,
1009 37(1), 840, 31 – 39, [https://doi.org/10.1016/0038-092X\(86\)90104-0](https://doi.org/10.1016/0038-092X(86)90104-0), 1986.
- 1010 Castelli, F., Entekhabi, D. and Caporali, E.: Estimation of surface heat flux and an index of soil
1011 moisture using adjoint-state surface energy balance, *Water Resour. Res.*, 35(10), 3115 – 3125,
1012 <https://doi.org/10.1029/1999WR900140>, 1999.
- 1013 ~~Dare-Idowu, O., Brut, A., Cuxart, J., Tallec, T., Rivalland, V., Zawilski, B., Ceschia, E. and~~
1014 ~~Jarlan, L.: Surface energy balance and flux partitioning of annual crops in south-western~~
1015 ~~France. *Agricultural and Forest Meteorology*, 308 – 309, 108529,~~
1016 ~~<https://doi.org/10.1016/j.agrformet.2021.108529>, 2021.~~
- 1017 Didan, K.: MOD13Q1 MODIS/Terra Vegetation Indices 16-Day L3 Global 250m SIN Grid
1018 V006., distributed by NASA EOSDIS Land Processes DAAC,
1019 doi:10.5067/MODIS/MOD13Q1.006, 2021-06-06, 2015.
- 1020 Donohue, R. J., Hume, I. H., Roderick, M. L., McVicar, T. R., Beringer, J., Hutley, L. B., Arndt,
1021 S. K.: Evaluation of the remote-sensing-based DIFFUSE model for estimating photosynthesis
1022 of vegetation, *Remote Sens. Environ.*, 155, 349–365, doi:10.1016/j.rse.2014.09.007, 2014.
- 1023 ~~Drori, R.; Dan, H.; Sprintsin, M.; Sheffer, E. Precipitation Sensitive Dynamic Threshold: A New~~
1024 ~~and Simple Method to Detect and Monitor Forest and Woody Vegetation Cover in Sub-Humid~~
1025 ~~to Arid Areas. *Remote Sens.*, 12, 1231, doi:10.3390/rs12081231, 2020.~~
- 1026 Duan, A., Wang, M., Lei, Y. and Cui, Y.: Trends in summer rainfall over China associated with
1027 the Tibetan Plateau sensible heat source during 1980–2008, *J. Clim.*, 26, 261–75,
1028 <https://doi.org/10.1175/JCLI-D-11-00669.1>, 2013.
- 1029 Duan, S., Li, Z., Cheng, J. and Leng, P.: Cross-satellite comparison of operational land surface
1030 temperature products derived from MODIS and ASTER data over bare soil surfaces. *ISPRS*

1031 J. Photogramm. Remote Sens., 126, 1-10, <https://doi.org/10.1016/j.isprsjprs.2017.02.003>,
1032 2017.

1033 Eswar, R., Sekhar, M., Bhattacharya, B. and Bandyopadhyay, S.: Spatial Disaggregation of Latent
1034 Heat Flux Using Contextual Models over India, Remote Sens., 9(9), 949,
1035 <https://doi.org/10.3390/rs9090949>, 2017.

1036 Friedl, M., McIver, D., Hodges, J., Zhang, X., Muchoney, D., Strahler, A., Woodcock, C., Gopal,
1037 S., Schneider, A., Cooper, A., Baccini, A., Gao, F. and Schaaf, C.: Global land cover mapping
1038 from MODIS: algorithms and early results, Remote Sens. Environ., 83(1-2), 287 – 302,
1039 [https://doi.org/10.1016/S0034-4257\(02\)00078-0](https://doi.org/10.1016/S0034-4257(02)00078-0), 2002.

1040 Gao, Z., Horton, R. and Liu, H. P.: Impact of wave phase difference between soil surface heat
1041 flux and soil surface temperature on soil surface energy balance closure, J. Geophys. Res.,
1042 115, D16112, doi:10.1029/2009JD013278, 2010.

1043 Hillel, D.: Introduction to Soil Physics, San Diego, US, ISBN 9780123485205, 1982.

1044 Hulley, G., Malakar, N., and Freepartner, R.: Moderate Resolution Imaging Spectroradiometer
1045 (MODIS) Land Surface Temperature and Emissivity Product (MxD21) Algorithm Theoretical
1046 Basis Document Collection-6. Pasadena, California: Jet Propulsion Laboratory, California
1047 Institute of Technology, 2016

1048 Isaac, P., Cleverly, J., McHugh, I., van Gorsel, E., Ewenz, C., and Beringer, J.: OzFlux data:
1049 network integration from collection to curation, Biogeosciences, 14, 2903–2928,
1050 doi:10.5194/bg-14-2903-2017, 2017.

1051 Jarvis, P.G. and McNaughton, K.G.: Stomatal Control of Transpiration – Scaling up from Leaf to
1052 Region, Adv. Ecol. Res., 15, 1-49, [https://doi.org/10.1016/S0065-2504\(08\)60119-1](https://doi.org/10.1016/S0065-2504(08)60119-1), 1986.

1053 Johansen, O.: Thermal conductivity of soils, PhD Thesis, University of Trondheim. Hanover, NH:
1054 Cold Regions Research and Engineering Laboratory, US Army Corps of Engineers, CRREL
1055 Draft English translation, <https://apps.dtic.mil/sti/pdfs/ADA044002.pdf>, 1975.

1056 Johnston, M., Andreu, A., Verfaillie, J., Baldocchi, D., and Moorcroft, P.: What lies beneath:
1057 Vertical temperature heterogeneity in a Mediterranean woodland savanna, Remote Sens.
1058 Environ., <https://doi.org/10.1016/j.rse.2022.112950>, 2022.

1059 Kiptala, J., Mohamed, Y., Mul, M. and Van der Zaag, P.: Mapping evapotranspiration trends using
1060 MODIS and SEBAL model in a data scarce and heterogeneous landscape in Eastern

1061 Africa, *Water Resour. Res.*, 49(12), 8495 – 8510, <https://doi.org/10.1002/2013WR014240>,
1062 2013.

1063 Kustas, W. and Anderson, M.: Advances in thermal infrared remote sensing for land surface
1064 modeling, *Agric. For. Meteorol.*, 149(12), 2071-2081,
1065 <https://doi.org/10.1016/j.agrformet.2009.05.016>, 2009.

1066 Lagouarde J.-P., Bhattacharya BK, Crébassol P., Gamet P., Babu SS, Boulet G., Briottet X.,
1067 Buddhiraju KM, Cherchali S., Dadou I., Dedieu G., Gouhier M., Hagolle O Irvine M., Jacob
1068 F., Kumar A., Kumar KK, Laignel B., Mallick K., Murthy CS, Olioso A., Otle C., Pandya
1069 MR, Raju PV, Roujean J.-L., Sekhar M., Shukla MV, Singh SK, Sobrino J., Ramakrishnan
1070 R.: The Indian-French Trishna Mission: Earth Observation in the Thermal Infrared with High
1071 Spatio-Temporal Resolution, IGARSS 2018 - 2018 IEEE International Geoscience and
1072 Remote Sensing Symposium, Institute of Electrical and Electronics Engineers (IEEE). USA,
1073 4078-4081, doi:10.1109/IGARSS.2018.8518720, 2018.

1074 Lagouarde, J., Bhattacharya, B., Crébassol, P., Gamet, P., Adlakha, D., Murthy, C., Singh, S.,
1075 Mishra, M., Nigam, R., Raju, P., Babu, S., Shukla, M., Pandya, M., Boulet, G., Briottet, X.,
1076 Dadou, I., Dedieu, G., Gouhier, M., Hagolle, O., Irvine, M., Jacob, F., Kumar, K., Laignel,
1077 B., Maisongrande, P., Mallick, K., Olioso, A., Otlé, C., Roujean, J., Sobrino, J.,
1078 Ramakrishnan, R., Sekhar, M. and Sarkar, S.: Indo-French high-resolution thermal infrared
1079 space mission for earth natural resources assessment and monitoring – concept and definition
1080 of TRISHNA, *ISPRS - International Archives of the Photogrammetry, Remote Sensing and*
1081 *Spatial Information Sciences*, XLII-3/W6, 403-407, 2019.

1082 Lu, L., Zhang, T., Wang, T. and Zhou, X.: Evaluation of Collection-6 MODIS Land Surface
1083 Temperature Product Using Multi-Year Ground Measurements in an Arid Area of Northwest
1084 China, *Remote Sens.*, 10(11), 1852, <https://doi.org/10.3390/rs10111852>, 2018.

1085 Mallick, K., & Bhattacharya, B.K., Chaurasia, S., Dutta, S., Nigam, R., Mukherjee J., Banerjee,
1086 S., Kar, G., Rao, V., Gadgil, A., Parihar, J.: Evapotranspiration using MODIS data and limited
1087 ground observations over selected agroecosystems in India, *Int. J. Remote Sens.*, 28(10),
1088 2091-2110, <https://doi.org/10.1080/01431160600935620>, 2007.

1089 Mallick, K., Bhattacharya, B. K., Rao, V. U. M., Reddy, D.R., Banerjee, S., Venkatesh, H. ,
1090 Pandey, V., Kar, G., Mukherjee, J., Vyas, S., Gadgil, A.S., Patel, N.K.: Latent heat flux
1091 estimation in clear sky days over Indian agroecosystems using noontime satellite remote

1092 sensing data, *Agric For Meteorol*, 149(10), 1646-1665,
1093 <https://doi.org/10.1016/j.agrformet.2009.05.006>, 2009.

1094 Mallick, K., Boegh, E., Trebs, I., Alfieri, J., Kustas, W., Prueger, J., Niyogi, D., Das, N., Drewry,
1095 D., Hoffmann, L. and Jarvis, A.: Reintroducing radiometric surface temperature into the
1096 Penman-Monteith formulation, *Water Resour. Res.*, 51(8), 6214 – 6243,
1097 <https://doi.org/10.1002/2014WR016106>, 2015a.

1098 Mallick, K., Jarvis, A., Boegh, E., Fisher, J., Drewry, D., Tu, K., Hook, S., Hulley, G., Ardö, J.,
1099 Beringer, J., Arain, A. and Niyogi, D.: A Surface Temperature Initiated Closure (STIC) for
1100 surface energy balance fluxes, *Remote Sens. Environ.*, 141, 243 – 261,
1101 <https://doi.org/10.1016/j.rse.2013.10.022>, 2014.

1102 Mallick, K., Jarvis, A., Wohlfahrt, G., Kiely, G., Hirano, T., Miyata, A., Yamamoto, S., and
1103 Hoffmann, L.: Components of near-surface energy balance derived from satellite soundings –
1104 Part 1: Noontime net available energy, *Biogeosci.*, 12, 433–451, [https://doi.org/10.5194/bg-](https://doi.org/10.5194/bg-12-433-2015)
1105 [12-433-2015](https://doi.org/10.5194/bg-12-433-2015), 2015.

1106 Mallick, K., Toivonen, E., Trebs, I., Boegh, E., Cleverly, J., Eamus, D., Koivusalo, H., Drewry,
1107 D., Arndt, S., Griebel, A., Beringer, J. and Garcia, M.: Bridging Thermal Infrared Sensing and
1108 Physically-Based Evapotranspiration Modeling: From Theoretical Implementation to
1109 Validation Across an Aridity Gradient in Australian Ecosystems, *Water Resour. Res.*, 54(5),
1110 3409 – 3435, <https://doi.org/10.1029/2017WR021357>, 2018a.

1111 Mallick, K., Trebs, I., Boegh, E., Giustarini, L., Schlerf, M., Drewry, D., Hoffmann, L., von
1112 Randow, C., Kruijt, B., Araùjo, A., Saleska, S., Ehleringer, J., Domingues, T., Ometto, J.,
1113 Nobre, A., de Moraes, O., Hayek, M., Munger, J. and Wofsy, S.: Canopy-scale biophysical
1114 controls of transpiration and evaporation in the Amazon Basin, *Hydrol. Earth Syst. Sci.*, 20,
1115 4237–4264, doi:10.5194/hess-20-4237-2016, 2016.

1116 Mallick, K., Wandera, L., Bhattarai, N., Hostache, R., Kleniewska, M. and Chormanski, J.: A
1117 Critical Evaluation on the Role of Aerodynamic and Canopy–Surface Conductance
1118 Parameterization in SEB and SVAT Models for Simulating Evapotranspiration: A Case Study
1119 in the Upper Biebrza National Park Wetland in Poland, *Water*, 10(12), 1753,
1120 <https://doi.org/10.3390/w10121753>, 2018b.

1121 [Mallick, K., Baldocchi, D., Jarvis, A., Hu, T., Trebs, I., Sulis, M., et al.: Insights into the](#)
1122 [aerodynamic versus radiometric surface temperature debate in thermal-based evaporation](#)

1123 [modeling. Geophys. Res. Let., 49, e2021GL097568. https://doi.org/10.1029/2021GL097568,](https://doi.org/10.1029/2021GL097568)
1124 [2022.](https://doi.org/10.1029/2021GL097568)

1125 Maltese, A., Bates, P., Capodici, F., Cannarozzo, M., Ciraolo, G. and La Loggia, G.: Critical
1126 analysis of thermal inertia approaches for surface soil water content retrieval, *Hydrol. Sci. J.*,
1127 58(5), 1144-1161, <https://doi.org/10.1080/02626667.2013.802322>, 2013.

1128 Martel, M., Glenn, A., Wilson, H. and Kröbel, R.: Simulation of actual evapotranspiration from
1129 agricultural landscapes in the Canadian Prairies, *J. Hydrol. Reg. Stud.*, 15, 105 – 118,
1130 <https://doi.org/10.1016/j.ejrh.2017.11.010>, 2018.

1131 Matheny, A., Bohrer, G., Stoy, P., Baker, I., Black, A., Desai, A., Dietze, M., Gough, C., Ivanov,
1132 V., Jassal, R., Novick, K., Schäfer, K. and Verbeeck, H.: Characterizing the diurnal patterns
1133 of errors in the prediction of evapotranspiration by several land-surface models: An NACP
1134 analysis, *J. Geophys. Res. Biogeosci.*, 119 (7), 1458 – 1473,
1135 <https://doi.org/10.1002/2014JG002623>, 2014.

1136 Minasny, B. & Hartemink, A. E.: Predicting soil properties in the tropics. *Earth-Science Rev.*, 1
1137 – 2, 52 – 62, <https://doi.org/10.1016/j.earscirev.2011.01.005>, 2011.

1138 [Mihailovic, D. T., Kallos, G., Aresenic, I.D., Lalic, B., Rajkovic, B. and Papadopoulos, A.:](https://doi.org/10.1016/j.earscirev.2011.01.005)
1139 [Sensitivity of soil surface temperature in a Force-Restore Equation to heat fluxes and deep](https://doi.org/10.1016/j.earscirev.2011.01.005)
1140 [soil temperature. *Intl. J. Climatol.*, 19, 1617-1632, 1999.](https://doi.org/10.1016/j.earscirev.2011.01.005)

1141 Monteith, J & Unsworth, M.: *Principles of Environmental Physics: Plants, Animals, and the*
1142 *Atmosphere*, Fourth Edition, 1-401, 2013.

1143 Moran, M. S., Jackson, R. D., Raymond, L. H., Gay, L. W. and Slater, P. N.: Mapping surface
1144 energy balance components by combining landsat thematic mapper and ground-based
1145 meteorological data, *Remote Sens. Environ.*, 30, 77 – 87, [https://doi.org/10.1016/0034-](https://doi.org/10.1016/0034-4257(89)90049-7)
1146 [4257\(89\)90049-7](https://doi.org/10.1016/0034-4257(89)90049-7), 1989.

1147 Morisson, R., Angadi, S. S., Cooper, H. M., Evans, J. G., Rees, G., Sekhar, M., Taylor, C.,
1148 Tripathi, S. N. and Turner, A. G. : Energy and carbon dioxide fluxes, meteorology and soil
1149 physics observed at INCOMPASS land surface stations in India, 2016 to 2017, NERC
1150 Environmental Information Data Centre, doi:10.5285/78c64025-1f8d-431cbdeb-
1151 e69a5877d2ed, 2019b.

1152 Morisson, R., Angadi, S. S., Cooper, H. M., Evans, J., Rees, G., Sekhar, M., Taylor, C., Tripathi,
1153 S. N. and Turner, A. G. : High temporal resolution meteorology and soil physics observations

1154 from INCOMPASS land surface stations in India, 2016 to 2018, NERC Environmental
1155 Information Data Centre, doi:10.5285/c5e72461-c61f-4800-8bbf-95c85f74c416, 2019a.

1156 Murray, T. and Verhoef, A.: Moving towards a more mechanistic approach in the determination
1157 of soil heat flux from remote measurements, *Agric. For. Meteorol.*, 147(1-2), 80 – 87,
1158 <https://doi.org/10.1016/j.agrformet.2007.06.009>, 2007.

1159 Norman, J., Anderson, M., Kustas, W., French, A., Mecikalski, J., Torn, R., Diak, G., Schugge,
1160 T. and Tanner, B.: Remote sensing of surface energy fluxes at 10¹-m pixel resolutions, *Water*
1161 *Resour. Res.* 39(8), <https://doi.org/10.1029/2002WR001775>, 2003.

1162 Purdy, A., Fisher, J., Goulden, M. and Famiglietti, J.: Ground heat flux: An analytical review of
1163 6 models evaluated at 88 sites and globally, *J. Geophys. Res.: Biogeosci.*, 121(12), 3045 –
1164 3059, <https://doi.org/10.1002/2016JG003591>, 2016.

1165 Raja, P., Singh, M., Singh, N., and Sinha, N.K.: Photosynthesis and Biomass studies in *Lasiurus*
1166 *indicus* of Chandan Grassland in Thar Desert, XXIII International Grassland Conference, New
1167 Delhi, Volume: IGC 2015, 2015.

1168 Santanello, J. and Friedl, M.: Diurnal Covariation in Soil Heat Flux and Net Radiation, *J. Appl.*
1169 *Meteorol.*, 42(6), 851 – 862, [https://doi.org/10.1175/1520-](https://doi.org/10.1175/1520-0450(2003)042<0851:DCISHF>2.0.CO;2)
1170 [0450\(2003\)042<0851:DCISHF>2.0.CO;2](https://doi.org/10.1175/1520-0450(2003)042<0851:DCISHF>2.0.CO;2), 2003.

1171 [Schmid, H.P.: Footprint modelling for vegetation atmosphere exchange studies: a review and](#)
1172 [perspective. *Agric. For. Meteorol.*, 113, 159-183, 2002.](#)

1173 Sauer T.J. and Horton, R.: Soil Heat flux, *Micrometeorology in Agricultural Systems*, Agronomy
1174 Monograph no. 47, American Society of Agronomy, Crop Science Society of America, Soil
1175 Science Society of America, 677 S. Segoe Rd., Madison, WI 53711, USA, 2005.

1176 Schaaf, C., Gao, F., Strahler, A., Lucht, W., Li, X., & Tsang, T. , trugnell, N. C., Zhang, X., Jin,
1177 Y., Muller, J., Lewis, P., Barnsley, M., Hobson, P., Disney, M., Roberts, G., Dunderdale, M.,
1178 Doll, C., d'Entremont, R. P., Hu, B., Liang, S., Privette, J. L. and Roy, D. : First operational
1179 BRDF, albedo nadir reflectance products from MODIS, *Remote Sens. Environ.*, 83 (1-2), 135-
1180 148, doi:10.1016/s0034-4257(02)00091-3, 2002.

1181 Schymanski, S. J., Breitenstein, D., and Or, D.: Technical note: An experimental set-up to measure
1182 latent and sensible heat fluxes from (artificial) plant leaves, *Hydrol. Earth Syst. Sci.*, 21, 3377–
1183 3400, <https://doi.org/10.5194/hess-21-3377-2017>, 2017.

1184 Singh, A.: *Integrated Water Management: Water and Plant Growth*, 1–16, 2007.

1185 Stoy, P., Mauder, M., Foken, T., Marcolla, B., Boegh, E., Ibrom, A., Arain, M., Arneth, A.,
1186 Aurela, M., Bernhofer, C., Cescatti, A., Dellwik, E., Duce, P., Gianelle, D., van Gorsel, E.,
1187 Kiely, G., Knohl, A., Margolis, H., McCaughey, H., Merbold, L., Montagnani, L., Papale, D.,
1188 Reichstein, M., Saunders, M., Serrano-Ortiz, P., Sottocornola, M., Spano, D., Vaccari, F. and
1189 Varlagin, A.: A data-driven analysis of energy balance closure across FLUXNET research
1190 sites: The role of landscape scale heterogeneity, *Agric. For. Meteorol.*, 171 – 172, 137 – 152,
1191 <https://doi.org/10.1016/j.agrformet.2012.11.004>, 2013.

1192 Su, Z.: The Surface Energy Balance System (SEBS) for estimation of turbulent heat fluxes,
1193 *Hydrol. Earth Syst. Sci.*, 6, 85–100, doi:10.5194/hess-6-85-2002, 2002.

1194 Tian, L., Zhang, Y., & Zhu, J.: Decreased surface albedo driven by denser vegetation on the
1195 Tibetan Plateau, *Environ. Res. Lett.*, 9(10), 104001, doi:10.1088/1748-9326/9/10/104001,
1196 2014.

1197 Trebs, I., Mallick, K., Bhattarai, N., Sulis, M., Cleverly, J., Woodgate, W., Silberstein, R., Najera,
1198 H.-N., Beringer, J., Meyer, W. S., Su, Z., and Boulet, G.: The role of aerodynamic resistance
1199 in thermal remote sensing-based evapotranspiration models, *Remote Sens. Environ.*, 264,
1200 112602, doi:10.1016/j.rse.2021.112602, 2021

1201 Tsuang, B.: Ground Heat Flux Determination according to Land Skin Temperature Observations
1202 from *in-situ* Stations and Satellites, *J. Hydrometeorol.*, 6(4), 371 – 390,
1203 <https://doi.org/10.1175/JHM425.1>, 2005.

1204 Turner, A., Bhat, G., Martin, G., Parker, D., Taylor, C., Mitra, A., Tripathi, S., Milton, S.,
1205 Rajagopal, E., Evans, J., Morrison, R., Pattnaik, S., Sekhar, M., Bhattacharya, B., Madan, R.,
1206 Govindankutty, M., Fletcher, J., Willetts, P., Menon, A. and Marsham, J.: Interaction of
1207 convective organization with monsoon precipitation, atmosphere, surface and sea: The 2016
1208 INCOMPASS field campaign in India, *Q. J. R. Meteorolog. Soc.*, 1–25,
1209 <https://doi.org/10.1002/qj.3633>, 2019.

1210 Van Dijk, A.I.J.M., Gash, J.H., Gorsel, E.V., Blanken, P.D., Cescatti, A., Emmel, C., Gielen, B.,
1211 Harman, I.N., Kiely, G., Merbold, L., Montagnani, L., Moors, E., Sottocornola, M., Varlagin,
1212 A., Williams, C.A., Wohlfahrt, G.: Rainfall interception and the coupled surface water and
1213 energy balance, *Agric For Meteorol.*, 214 – 215, 402 – 415,
1214 <https://doi.org/10.1016/j.agrformet.2015.09.006>, 2015.

- 1215 Van Genuchten, M.: A Closed-form Equation for Predicting the Hydraulic Conductivity of
1216 Unsaturated Soils, *Soil Sci. Soc. Am. J.*, 44(5), 892,
1217 <https://doi.org/10.2136/sssaj1980.03615995004400050002x>, 1980.
- 1218 Venturini, V., Islam, S. and Rodriguez, L.: Estimation of evaporative fraction and
1219 evapotranspiration from MODIS products using a complementary based model, *Remote Sens.*
1220 *Environ.*, 112(1), 132 – 141, doi:10.1016/j.rse.2007.04.014, 2008.
- 1221 Verhoef, A., Ottlé, C., Cappelaere, B., Murray, T., Saux-Picart, S., Zribi, M., Maignan, F.,
1222 Boulain, N., Demarty, J. and Ramier, D.: Spatio-temporal surface soil heat flux estimates from
1223 satellite data; results for the AMMA experiment at the Fakara (Niger) supersite, *Agric. For.*
1224 *Meteorol.*, 154-155, 55 – 66, doi:10.1016/j.agrformet.2011.08.003, 2012.
- 1225 Verhoef, A.: Remote estimation of thermal inertia and soil heat flux for bare soil, *Agric. For.*
1226 *Meteorol.*, 123(3-4), 221 – 236, doi:10.1016/j.agrformet.2003.11.005, 2004.
- 1227 [Vesala, T., Kljun, N., Rannik, U., Rinne, A. Sogachev, Markkanen, T., Sabelfeld, K., Foken, T.](#)
1228 [and Leclerc, M.Y.: Flux and concentration footprint modelling: State of the art. *Environ.*](#)
1229 [Polln.](#), 152, 653-666, 2008.
- 1230 Wan, Z.: New refinements and validation of the collection-6 MODIS land-surface
1231 temperature/emissivity product, *Remote Sens. Environ.*, 140, 36 – 45,
1232 doi:10.1016/j.rse.2013.08.027, 2014.
- 1233 Wang, S., Yang, Y., Luo, Y., and Rivera, A.: Spatial and seasonal variations in evapotranspiration
1234 over Canada's landmass, *Hydrol. Earth Syst. Sci.*, 17, 3561–3575, doi:10.5194/hess-17-3561-
1235 2013, 2013.
- 1236 Wilson, K., Goldstein, A., Falge, E., Aubinet, M., Baldocchi, D., Berbigier, P., Bernhofer, C.,
1237 Ceulemans, R., Dolman, H., Field, C., Grelle, A., Ibrom, A., Law, B., Kowalski, A., Meyers,
1238 T., Moncrieff, J., Monson, R., Oechel, W., Tenhunen, J., Valentini, R. and Verma, S.: Energy
1239 balance closure at FLUXNET sites, *Agric. For. Meteorol.*, 113(1-4), 223 – 243,
1240 doi:10.1016/S0168-1923(02)00109-0, 2002.
- 1241 Winter, J. and Eltahir, E.: The Sensitivity of Latent Heat Flux to Changes in the Radiative Forcing:
1242 A Framework for Comparing Models and Observations, *J. Clim.*, 23(9), 2345-2356,
1243 doi:10.1175/2009JCLI3158.1, 2010.
- 1244 Zerefos, C. S. & Bais, A. F.: *Solar Ultraviolet Radiation: Modelling, Measurements and Effects*,
1245 Springer Berlin Heidelberg, 2013.

1246 ~~Xue, J. & Su, B.: Significant Remote Sensing Vegetation Indices: A Review of Developments~~
 1247 ~~and Applications. J. Sens., 1-17, doi:10.1155/2017/1353691, 2017.~~

1248 **Appendix A**

1249 **Table A1: A list of symbols, their descriptions and units used in the present study**

Attributes	Symbol	Description
Temperature	T_A	Air temperature ($^{\circ}\text{C}$)
	T_{Max}	Maximum air temperature ($^{\circ}\text{C}$)
	T_{Min}	Minimum air temperature ($^{\circ}\text{C}$)
	T_D	Air dew-point temperature ($^{\circ}\text{C}$)
	T_{STA}	point-scale soil temperature amplitude
	ΔT_s	noon-night LST difference ($^{\circ}\text{C}$)
	T_{ST}	Soil temperature ($^{\circ}\text{C}$)
Humidity, vapor pressures	R_H	Relative humidity (%)
	e_A	Atmospheric vapor pressure at the level of T_A measurement (hPa)
	e_A^*	Saturation vapor pressure at the level of T_A measurement (hPa)
	e_s^*	Saturation vapor pressure at surface (hPa)
	D_A	Atmospheric vapor pressure deficit at the level of T_A measurement (hPa)
Radiation	R_G	Downwelling shortwave radiation (or global radiation) (W m^{-2})
	R_R	Upwelling or reflected shortwave radiation (W m^{-2})
	$R_{L\downarrow}$	Downwelling longwave radiation (W m^{-2})

	$R_{L\uparrow}$	Upwelling longwave radiation ($W m^{-2}$)
	τ_{sw}	Atmospheric transmissivity for shortwave radiation (unitless)
	α_R	Broadband shortwave surface albedo (unitless)
SEB components	LE_i	Latent heat flux ($W m^{-2}$); subscript 'i' signifies 'instantaneous'
	H_i	Sensible heat flux ($W m^{-2}$); subscript 'i' signifies 'instantaneous'
	G_i	Ground heat flux ($W m^{-2}$); subscript 'i' signifies 'instantaneous'
	R_{Ni}	Net radiation ($W m^{-2}$); subscript 'i' signifies 'instantaneous'
	ϕ	Net available energy ($W m^{-2}$); i.e., $R_N - G$
MV2007 model	A	Ecosystem-scale surface soil temperature amplitude ($^{\circ}C$)
	T_{Sd}	Daytime T_S ($^{\circ}C$)
	T_{Sn}	Nighttime T_S ($^{\circ}C$)
	ω	Angular frequency ($rad s^{-1}$)
	ϕ'_n	Phase shift of the n^{th} soil surface temperature harmonic (rad)
	Δ	Shape parameter (unitless)
	S_r	Relative soil moisture saturation ($m^3 m^{-3}$)
	f_s	Sand fraction (unitless)
	θ_{fc}	Soil water content at field capacity ($m^3 m^{-3}$)
	θ_{wp}	Soil water content at permanent wilting point ($m^3 m^{-3}$)
	θ^*	Soil porosity ($cm^3 cm^{-3}$)
	J_s	Summation of harmonic terms of soil surface temperature (K)
	γ'	Soil textural parameter (unitless)
Γ	Soil thermal inertia ($J K^{-1} m^{-2} s^{-0.5}$)	

	τ_0	Thermal inertia of air-dry soil ($\text{J K}^{-1} \text{m}^{-2} \text{s}^{-0.5}$)
	τ^*	Thermal inertia of saturated soil ($\text{J K}^{-1} \text{m}^{-2} \text{s}^{-0.5}$)
	t'	Time of satellite overpass (seconds)
	Δt	Time offset between the canopy composite temperature and the below-canopy soil surface temperature (seconds)
	κ	Total number of harmonics used (unitless)
	f_c	Vegetation fraction (unitless)
	θ	Volumetric soil moisture (cm cm^{-3})
Clear-sky R_{Ni} model	R_{ns}	Net shortwave radiation (W m^{-2})
	R_{nl}	Net long wave radiation (W m^{-2})
	G_{sc}	Solar constant (1367 W m^{-2})
	β_e	Sun elevation angle ($^\circ$).
	ε_s	Infrared surface emissivity (unitless)
	ε_a	Atmospheric emissivity (unitless)
	E	Eccentricity correction factor due to variation in Sun-Earth distance (unitless)
	M	Aggregated moisture availability (0-1)
	g_A	Aerodynamic conductance (m s^{-1})
	g_s	Canopy-surface conductance (m s^{-1})
	T_0	Aerodynamic temperature (or source/sink height temperature) ($^\circ\text{C}$)
	T_{0D}	Dewpoint temperature at the source/sink height ($^\circ\text{C}$)
	Λ	Evaporative fraction (unit less)

STIC-TI model	e_0	Vapor pressure at the source/sink height (hPa)
	e_0^*	Saturation vapor pressure at the source/sink height (hPa)
	D_0	Vapor pressure deficit at source/sink height (hPa)
	s_1	Psychrometric slope of vapor pressure and temperature between (T_{0D} - T_D) versus ($e_0 - e_A$) (h Pa K^{-1})
	s_2	Psychrometric slope of vapor pressure and temperature between ($T_s - T_D$) versus ($e_s^* - e_A$) (h Pa K^{-1})
	s_3	Psychrometric slope of vapor pressure and temperature between ($T_{0D} - T_D$) versus ($e_s^* - e_A$).
	κ	Ratio between ($e_0^* - e_A$) and ($e_s^* - e_A$) (unitless)
	s	Slope of saturation vapor pressure vs. temperature curve (h Pa K^{-1})
	α	Priestley-Taylor coefficient (unitless)
Ancillary meteorological variables	U	Wind speed at 8 m height ($m s^{-1}$)
	u^*	Friction velocity ($m s^{-1}$)
Constants	P	Precipitation ($mm d^{-1}$)
	γ	Psychrometric constant (h Pa k^{-1})
	c_p	Specific heat capacity of air at constant pressure ($MJ kg^{-1} K^{-1}$)
	ρ	Density of air ($Kg m^{-3}$)
	σ	Stefan–Boltzmann constant ($5.67 \times 10^{-8} Wm^{-2}K^{-4}$)

1251 **Table A2:** Summary of instruments used, height or depth and period of measurements, measured
 1252 variables at nine EC flux tower sites

Type of primary instruments used for in situ data recording at flux tower sites	Measurement Height/ Depth (m) at different sites	Measured variables
Net radiometer	<ul style="list-style-type: none"> • 3m (IND-Naw, IND-Jai, IND-Sam) • 15m (AU-Ade) • 12.2m (AU-ASM) • 23m (AU-How) 2m (US-Ton, US-Var) 	Four radiation flux components: shortwave incoming (R_G) and outgoing (R_R); longwave incoming ($R_{L\downarrow}$) and outgoing ($R_{L\uparrow}$)
EC assembly with IRGA (Infrared Gas Analyzer), three-dimensional sonic anemometer, TC probe	<ul style="list-style-type: none"> • 8m (IND-Naw; IND-Jai; IND-Sam) • 4.5m (IND-Dha) • 15m (AU-Ade) • 11.6m (AU-ASM) • 23m (AU-How) • 2m (US-Ton, US-Var) 	High response wind vectors (u , v and w), sonic temperature, and CO_2 - water vapor mass at 10/20 Hz frequency
Humidity and temperature probe	<ul style="list-style-type: none"> • 8m (IND-Naw, IND-Jai, IND-Sam) • 4.5m (IND-Dha) • 15m (AU-Ade), 11.6m (AU-ASM) • 23m (AU-How), 70m (AU-How) • 2m (US-Ton, US-Var) 	T_A and R_H
Soil temperature probe	<ul style="list-style-type: none"> • -0.1m (IND-Dha) • -0.15m (AU-Ade) • (-0.02, -0.06m) (AU-ASM) • -0.08m (AU-How) • -0.02m, -0.04m, -0.08m, and -0.16m (US-Ton, US-Var) 	T_{ST}
Soil heat flux plates	<ul style="list-style-type: none"> • Ground, 0.1 m (IND-Dha) • Ground, -0.15 m (AU-Ade) • Ground, -0.08 m (AU-ASM) • Ground, -0.15 m (AU-How) • -0.01m (US-Ton, US-Var) 	Soil heat flux (G)

1253 **Appendix B**

1254 **B1: Clear-sky instantaneous net radiation (R_{Ni}) model**

1255 Net radiation (R_N) is defined as the difference between the incoming and outgoing radiation fluxes,
 1256 which includes both longwave and shortwave radiation at the surface of earth.

1257 Terrestrial R_N has four components: downwelling and upwelling shortwave radiation (R_G and R_R),
 1258 downwelling and upwelling longwave radiation ($R_{L\downarrow}$ and $R_{L\uparrow}$), respectively.

$$R_N = (R_G - R_R) + (R_{L\downarrow} - R_{L\uparrow}) \quad (B1)$$

1259 Out of these four terms mentioned in eq.(B1), R_G and $R_{L\downarrow}$ are dependent on various factors such
 1260 as geographic location, season, cloudiness, aerosol loading, atmospheric water vapor content and
 1261 less on surface properties. On the other hand, the upwelling radiations in eq. (B1) strongly depends
 1262 on the surface properties such as surface reflectance and emittance, land surface temperature, and
 1263 soil water content (Zerefos and Bais, 2013).

1264 Instantaneous net radiation (R_{Ni}) can be derived using eq. B2 as follows (Mallick et al., 2007):

$$R_{Ni} = R_{ns} - R_{nl} \quad (B2)$$

$$R_{ns} = (1 - \alpha_R) R_G \quad (B3)$$

$$R_{nl} = R_{L\downarrow} - R_{L\uparrow} \quad (B4)$$

1265 Where, R_{ns} is net shortwave radiation ($W m^{-2}$), R_{nl} is net longwave radiation ($W m^{-2}$).and α_R is
 1266 the broadband surface albedo shortwave spectrum.

1267 A WMO (World Meteorological Organization) shortwave radiation model (Cano et al.,1986)
 1268 calibrated over Indian conditions (Mallick et al., 2007, 2009) was used to compute R_G using the
 1269 following equation:

$$R_G = \tau_{sw} G_{sc} E (\sin\beta_e)^{1.15} \quad (B5)$$

1270 Where, τ_{sw} is the is the global clear sky transmissivity for the shortwave radiation (0.7), G_{sc} is the
 1271 solar constant ($1367 Wm^{-2}$), ϵ is the eccentricity correction factor due to variation in Sun-Earth
 1272 distance and β_e is the sun elevation in degrees.

1273 $R_{L\downarrow}$ at any instance was calculated as follows:

$$R_{L\downarrow} = \epsilon_a \sigma (273.14 + T_A)^4 \quad (B6)$$

1274 Where, σ is the Stefan–Boltzmann constant ($5.67 \times 10^{-8} \text{ Wm}^{-2}\text{K}^{-4}$); T_A is the air temperature ($^{\circ}\text{C}$);
1275 ϵ_a is the atmospheric emissivity.

1276 Atmospheric emissivity (ϵ_a) was computed using the following equation (Bastiaanssen et
1277 al.,1998):

$$\epsilon_a = 0.85 - \ln\tau_{\text{sw}}^{0.09} \quad (\text{B7})$$

1278 $R_{L\uparrow}$ at any particular instance was calculated as follows:

$$R_{L\uparrow} = \epsilon_s \sigma (273.14 + T_s)^4 \quad (\text{B8})$$

1279 Where, ϵ_s is the surface emissivity in thermal infrared (8 – 14 μm) spectrum and T_s is the land
1280 surface temperature ($^{\circ}\text{C}$).

1281 **B2: Evaluation of STIC-TI R_{Ni}**

1282 Comparison of the clear-sky R_{Ni} estimates with respect to *in situ* measurements revealed RMSE in
1283 R_{Ni} to the order of 27 – 72 W m^{-2} , MAPD 8 –24%, BIAS (-67) – 50 W m^{-2} , and R^2 varying from
1284 0.62– 0.90 across all the sites (Fig. B2, Table B2). Among the nine sites, a consistent
1285 underestimation of R_{Ni} was noted in IND-Dha, US-Ton, and US-Var (with BIAS of -23 W m^{-2} , -
1286 61 W m^{-2} and -67 W m^{-2}), whereas substantial overestimation of R_{Ni} was found in IND-Sam, IND-
1287 Naw, and AU-ASM with a BIAS of 50 W m^{-2} , 37 W m^{-2} and 43 W m^{-2} , respectively (Table B2).

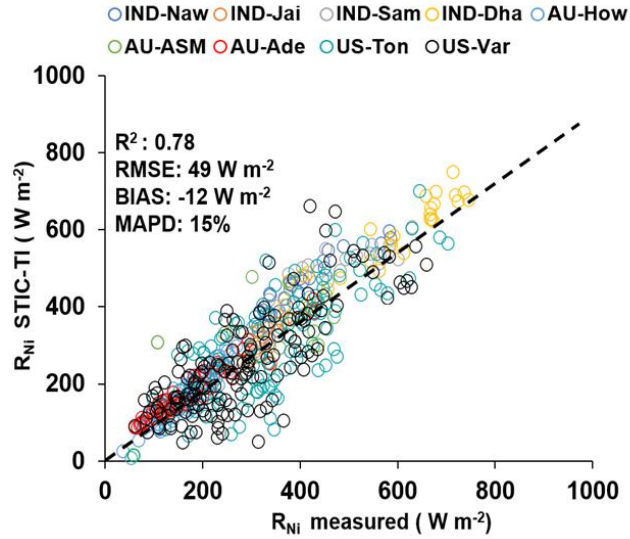


Figure B2: Validation of STIC-TI derived R_{Ni} estimates with respect to *in situ* measurements in different ecosystems. The regression equation between modeled versus in-situ R_{Ni} is, R_{Ni} (STIC-TI) = 0.78 R_{Ni} (tower) +58.92.

1288 **Table B2:** Performance evaluation statistics of clear-sky R_{Ni} estimates in nine different
1289 agroecosystems

Sites	Error statistics of clear-sky R_{Ni} model estimates			
	R^2	BIAS ($W m^{-2}$)	RMSE ($W m^{-2}$)	MAPD (%)
IND-Jai	0.81	-9	32	8
IND-Naw	0.81	37	56	12
IND-Dha	0.81	-23	42	9
IND-Sam	0.64	50	67	15
US-Ton	0.68	-61	69	21
US-Var	0.62	-67	72	24
Au-How	0.87	7	27	15
AU-ASM	0.88	43	50	14
AU-Ade	0.90	11	27	16

1290 **Appendix C**

1291 **C1: Estimating SEB fluxes using STIC1.2 analytical model and thermal remote sensing data**

1292 STIC1.2 (Mallick et al., 2014, 2015a,b, 2016, 2018a) is a one-dimensional physically based SEB
1293 model and is based on the integration of satellite LST observations into the Penman–Monteith
1294 Energy Balance (PMEB) equation (Monteith, 1965). In STIC1.2, the vegetation–substrate
1295 complex is considered as a single slab. Therefore, the aerodynamic conductances from individual
1296 air-canopy and canopy-substrate components is regarded as an ‘effective’ aerodynamic
1297 conductance (g_A), and surface conductances from individual canopy (stomatal) and substrate
1298 complexes is regarded as an ‘effective’ canopy-surface conductance (g_S) which simultaneously
1299 regulate the exchanges of sensible and latent heat fluxes (H and LE) between surface and
1300 atmosphere. One of the fundamental assumptions in STIC1.2 is the first order dependence of these
1301 two critical conductances on M through T_S . Such an assumption enabled an integration of satellite
1302 LST in the PMEB model (Mallick et al., 2016). The common expression for LE and H according
1303 to the PMEB equation is as follows:

$$LE = \frac{s\phi + \rho c_P g_A D_A}{s + \gamma \left(1 + \frac{g_A}{g_S}\right)} \quad (C6)$$

$$H = \frac{\gamma\phi \left(1 + \frac{g_A}{g_S}\right) - \rho c_P g_A D_A}{s + \gamma \left(1 + \frac{g_A}{g_S}\right)} \quad (C7)$$

1304 In the above equations, the two biophysical conductances (g_A and g_S) are unknown and the
1305 STIC1.2 methodology is based on finding analytical solutions for the two unknown conductances
1306 to directly estimate LE (Mallick et al., 2016, 2018a). The need for such analytical estimation of
1307 these conductances is motivated by the fact that g_A and g_S can neither be measured at the canopy
1308 nor at larger spatial scales, and there is no universally agreed appropriate model of g_A and g_S that
1309 currently exists (Matheny et al., 2014; van Dijk et al., 2015). By integrating T_S with standard SEB
1310 theory and vegetation biophysical principles, STIC1.2 formulates multiple state equations in order

1311 to eliminate the need to use the empirical parameterizations of the g_A and g_S and also to bypass the
 1312 scaling uncertainties of the leaf-scale conductance functions to represent the canopy-scale
 1313 attributes. The state equations for the conductances are expressed as a function of those variables
 1314 that are mostly available as remote sensing observations and weather forecasting models. In the
 1315 state equations, a direct connection to T_S is established by estimating M as a function of T_S . The
 1316 information of M is subsequently used in the state equations of conductances, aerodynamic
 1317 variables (aerodynamic temperature, aerodynamic vapor pressure), and evaporative fraction,
 1318 which is eventually propagated into their analytical solutions. M is a unitless quantity, which
 1319 describes the relative wetness (or dryness) of a surface and also controls the transition from
 1320 potential to actual evaporation; which implies $M \rightarrow 1$ under saturated surface conditions and $M \rightarrow 0$
 1321 under extremely dry conditions. Therefore, M is critical for providing a constraint against which
 1322 the conductances are estimated. Since T_S is extremely sensitive to the surface moisture variations,
 1323 it is extensively used for estimating M in a physical retrieval scheme (detail in Appendix A3 of
 1324 Bhattarai et al., 2018; Mallick et al., 2016, 2018a). It is hypothesized that linking M with the
 1325 conductances will simultaneously integrate the information of T_S into the PMEB model. To
 1326 illustrate, we express the state equations by symbols, $sv_1 = f \{c_1, c_2, c_3, v_1, v_2, v_3, v_4, sv_3, sv_5\}$; sv_2
 1327 $= f \{v_4, sv_1, sv_5, sv_6\}$; $sv_3 = f \{c_3, v_3, v_4, sv_4, sv_5\}$; $sv_4 = f \{c_3, v_3, sv_1, sv_2, sv_7, sv_8\}$. Here, f , sv , v ,
 1328 and c denote the function, state variables, input variables (5 input variables; radiative and
 1329 meteorological), and constants (3 constants), respectively. Here sv_1 to sv_4 are g_A , g_S , aerodynamic
 1330 temperature (T_0), evaporative fraction (Λ), and sv_8 is M . Given the estimates of M , net radiative
 1331 energy ($R_{Ni} - G_i$), T_A , R_H , the four state equations are solved simultaneously to derive analytical
 1332 solutions for the four state variables and to produce a surface energy balance “closure” that is
 1333 independent of empirical parameterizations for g_A , g_S , T_0 , and Λ . However, the analytical solutions
 1334 to the four state equations contain three accompanying unknown state variables (effective vapor
 1335 pressures at source/sink height, and Priestley-Taylor variable), and as a result there are four
 1336 equations with seven unknowns. Consequently, an iterative solution was found to determine the
 1337 three additional unknown variables as detailed in this section above and also described in Mallick
 1338 et al. (2016, 2018a) and Bhattarai et al. (2018). The state equations of STIC are given below.

$$g_A = \frac{\phi}{\rho_{CP} \left[(T_0 - T_A) + \left(\frac{e_0 - e_A}{\gamma} \right) \right]} \quad (C1)$$

$$g_S = g_A \frac{(e_0 - e_A)}{(e_0^* - e_0)} \quad (C2)$$

$$T_0 = T_A + \left(\frac{e_0 - e_A}{\gamma} \right) \left(\frac{1 - \Lambda}{\Lambda} \right) \quad (C3)$$

$$\Lambda = \frac{2\alpha s}{2s + 2\gamma + \gamma \frac{g_A}{g_S} (1 + M)} \quad (C4)$$

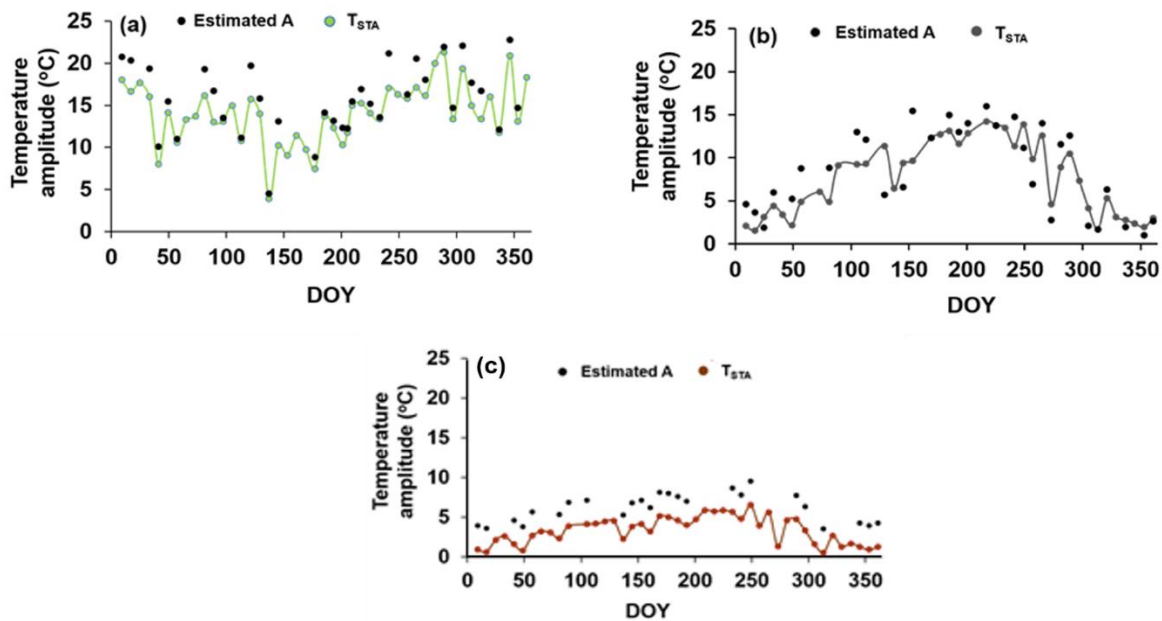
1339 Detailed derivations of these four state equations are given in Mallick et al. (2016). Given the
 1340 values of M , R_N , G , T_A , and R_H or e_A , the four state equations can be solved simultaneously to
 1341 derive analytical solutions for the four unobserved variables and to simultaneously produce a
 1342 ‘closure’ of the PMEB model that is independent of empirical parameterizations for both g_A and
 1343 g_S . However, the analytical solutions to the four state equations contain three accompanying
 1344 unknowns; e_0 (vapor pressure at the source/sink height), e_0^* (saturation vapor pressure at the
 1345 source/sink height), and Priestley-Taylor coefficient (α), and as a result there are four equations
 1346 with seven unknowns. Consequently, an iterative solution was needed to determine the three
 1347 unknown variables (as described in Appendix A2 in Mallick et al. 2016). Once the analytical
 1348 solutions of g_A and g_S are obtained, both variables are returned into eq. (13) to directly estimate
 1349 LE.

1350 In STIC-TI, an initial value of α was assigned as 1.26; initial estimates of e_0^* were obtained from
 1351 T_s through temperature-saturation vapour pressure relationship, and initial estimates of e_0 were
 1352 obtained from M as, $e_0 = e_A + M(e_0^* - e_A)$. Initial T_{0D} and M were estimated according to
 1353 Venturini et al. (2008) as described in section 3.2, and initial estimation of G was performed from
 1354 initial M using the equation sets eq. (2) – eq. (11). With the initial estimates of these variables;
 1355 first estimate of the conductances, T_0 , Λ , H , and LE were obtained. The process was then iterated
 1356 by updating e_0^* , D_0 , e_0 , T_{0D} , M , and α (using eq. A9, A10, A11, A17, A16 and A15 in Mallick et
 1357 al., 2016), with the first estimates of g_S , g_A , T_0 , and LE, and re-computing G , ϕ , g_S , g_A , T_0 , Λ , H ,
 1358 and LE in the subsequent iterations with the previous estimates of e_0^* , e_0 , T_{0D} , M , and α until the

1359 convergence of LE was achieved. Stable values of G, conductances, LE, H, T_0 , e_0^* , e_0 , T_{0D} , M, and
1360 α were obtained within ~25 iterations. The inputs needed for computation of LE_i (eq.C6) are air
1361 temperature (T_A), land surface temperature (T_S), relative humidity (R_H), net radiation (R_{Ni}) and
1362 soil heat flux (G_i).

1363 Appendix D

1364 The temporal variation of estimated A and T_{STA} is shown in Fig. D1. The annual variations of T_{STA}
1365 in different ecosystem was found to be within the ranges of 1 - 4°C.



1366
1367 **Figure D1:** Temporal variation of A and T_{STA} in (a) AU-ASM (2013), (b) US-Ton (2014), (c) US-
1368 Var (2014).

1369
1370
1371
1372

1373 **Appendix E**

1374 **Table E1:** Soil textural properties and their values used in the present study (Murray and Verhoef,
 1375 2007; Minasny et al., 2011; Anderson et al., 2007)

Soil texture	Water retention Shape parameter (δ)	Field capacity (vol/vol) (%) θ_{fc}	Wilting point (vol/vol) (%) θ_{wp}	Sand fraction (f_s)	Saturated soil moisture (vol/vol) (%) θ^*
Sand	2.77	10	5	0.92	43
Loamy Sand	2.39	12	5	0.82	41
Sandy loam	2.27	18	8	0.58	41
Loam	2.20	28	14	0.43	43
Silty loam	2.22	31	11	0.17	45
Sandy clay loam	2.17	27	17	0.58	39
Clay loam	2.14	36	22	0.40	41
Silty clay loam	2.14	38	22	0.10	43
Sandy clay	2.11	36	25	0.52	38
Silty clay	2.12	41	27	0.06	46
Clay	2.10	42	30	0.22	38

1376

1377

1378 **Appendix F**

1379 Day view angle effect on deviations of STIC-TI heat flux estimates from measurements is shown
1380 in Figure F.

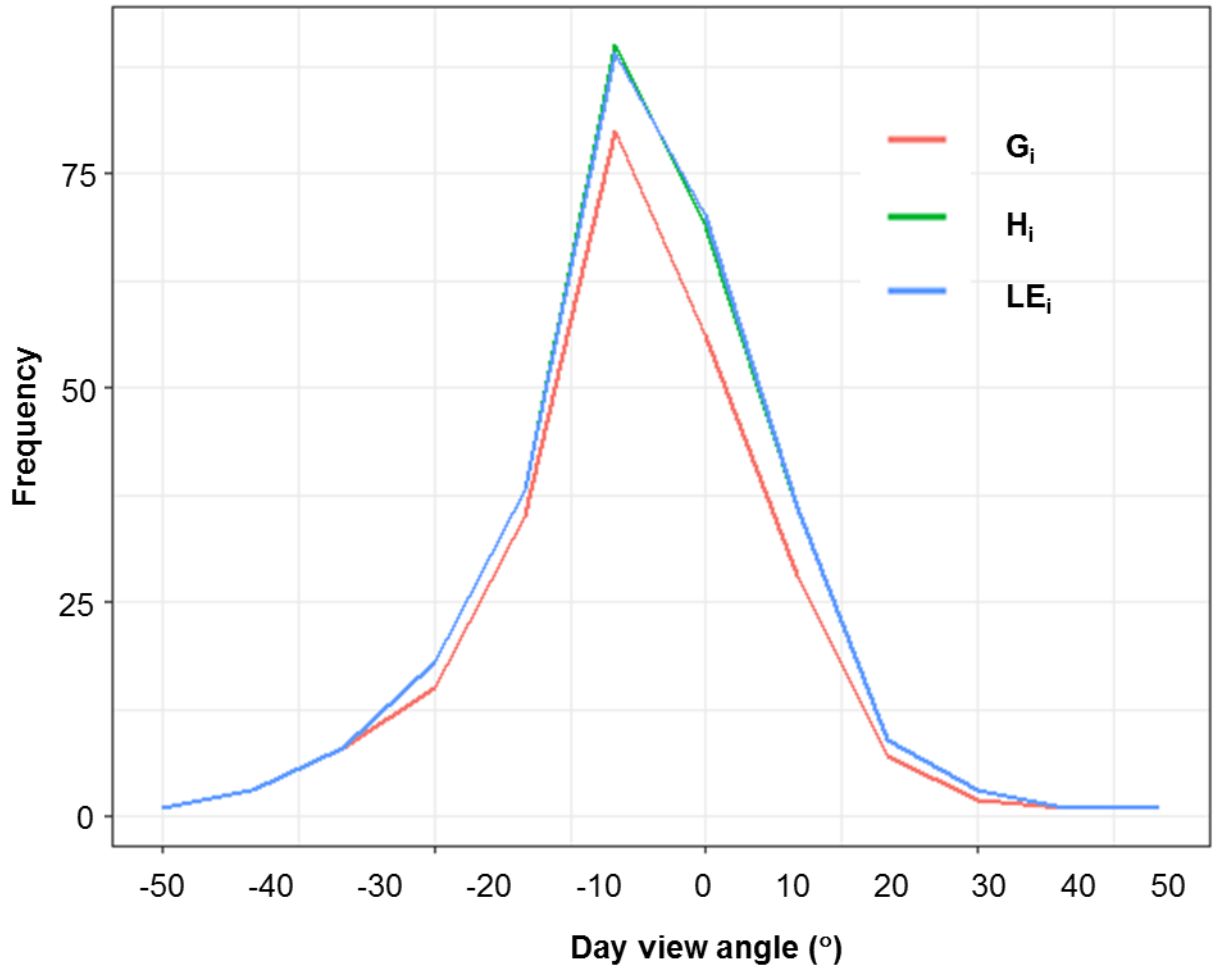


Figure F. Number of occurrences of deviations of STIC-TI heat flux estimates (G_i , H_i , LE_i) from measurements in each 10° bin within $\pm 50^\circ$ day view angle of MODIS Aqua

1381